



Direct reflectance transformation methodology for drone-based hyperspectral imaging

Juha Suomalainen^{*}, Raquel A. Oliveira, Teemu Hakala, Niko Koivumäki, Lauri Markelin, Roope Näsi, Eija Honkavaara

Department of Remote Sensing and Photogrammetry, Finnish Geospatial Research Institute, National Land Survey of Finland, Finland

ARTICLE INFO

Jing M. Chen

Keywords:

Remote sensing
Drone
UAV
Hyperspectral
Imaging
Direct reflectance
Atmospheric correction
Empirical line method
Radiometric calibration
Reflectance factor
Irradiance
Radiance

ABSTRACT

Multi- and hyperspectral cameras on drones can be valuable tools in environmental monitoring. A significant shortcoming complicating their usage in quantitative remote sensing applications is insufficient robust radiometric calibration methods. In a direct reflectance transformation method, the drone is equipped with a camera and an irradiance sensor, allowing transformation of image pixel values to reflectance factors without ground reference data. This method requires the sensors to be calibrated with higher accuracy than what is usually required by the empirical line method (ELM), but consequently it offers benefits in robustness, ease of operation, and ability to be used on Beyond-Visual Line of Sight flights. The objective of this study was to develop and assess a drone-based workflow for direct reflectance transformation and implement it on our hyperspectral remote sensing system. A novel atmospheric correction method is also introduced, using two reference panels, but unlike in the ELM, the correction is not directly affected by changes in the illumination. The sensor system consists of a hyperspectral camera (Rikola HSI, by Senop) and an onboard irradiance spectrometer (FGI AIRS), which were both given thorough radiometric calibrations. In laboratory tests and in a flight experiment, the FGI AIRS tilt-corrected irradiances had accuracy better than 1.9% at solar zenith angles up to 70°. The system's low-altitude reflectance factor accuracy was assessed in a flight experiment using reflectance reference panels, where the normalized root mean square errors (NRMSE) were less than $\pm 2\%$ for the light panels (25% and 50%) and less than $\pm 4\%$ for the dark panels (5% and 10%). In the high-altitude images, taken at 100–150 m altitude, the NRMSEs without atmospheric correction were within 1.4%–8.7% for VIS bands and 2.0%–18.5% for NIR bands. Significant atmospheric effects appeared already at 50 m flight altitude. The proposed atmospheric correction was found to be practical and it decreased the high-altitude NRMSEs to 1.3%–2.6% for VIS bands and to 2.3%–5.3% for NIR bands. Overall, the workflow was found to be efficient and to provide similar accuracies as the ELM, but providing operational advantages in such challenging scenarios as in forest monitoring, large-scale autonomous mapping tasks, and real-time applications. Tests in varying illumination conditions showed that the reflectance factors of the gravel and vegetation targets varied up to 8% between sunny and cloudy conditions due to reflectance anisotropy effects, while the direct reflectance workflow had better accuracy. This suggests that the varying illumination conditions have to be further accounted for in drone-based in quantitative remote sensing applications.

1. Introduction

The use of light-weight multi- and hyperspectral camera technologies are increasing rapidly in different applications. Combining these cameras with drones, also known as Unmanned Aerial Vehicles (UAV),

can offer great prospects for various mapping and monitoring applications, such as forest health (Wallace et al., 2012; Näsi et al., 2015; Dash et al., 2017), precision agriculture (Jay et al., 2019; Oliveira et al., 2020) and mineral mapping (Jakob et al., 2017). There exists a number of technical implementations of miniaturized hyperspectral cameras

^{*} Corresponding author at: Department of Remote Sensing and Photogrammetry, Finnish Geospatial Research Institute FGI, National Land Survey of Finland, P.O. Box 84, FI-00521 Helsinki, Finland.

E-mail addresses: juha.suomalainen@nls.fi (J. Suomalainen), raquel.alvesdeoliveira@nls.fi (R.A. Oliveira), teemu.hakala@nls.fi (T. Hakala), niko.koivumaki@nls.fi (N. Koivumäki), lauri.markelin@nls.fi (L. Markelin), roope.nasi@nls.fi (R. Näsi), eija.honkavaara@nls.fi (E. Honkavaara).

<https://doi.org/10.1016/j.rse.2021.112691>

Received 8 March 2021; Received in revised form 20 August 2021; Accepted 5 September 2021

Available online 11 September 2021

0034-4257/© 2021 The Authors. Published by Elsevier Inc. This is an open access article under the CC BY license (<http://creativecommons.org/licenses/by/4.0/>).

suitable for drone use, including hyperspectral pushbroom cameras by companies such as Headwall (Headwall Photonics, 2020) and SPECIM (SPECIM, 2020) and 2D cameras, for example, Senop (Senop, 2020), Cubert (Cubert, 2020), and Ximea (Ximea, 2020). Earlier research has shown that such hyperspectral cameras can be useful and accurate tools in drone-based remote sensing (Honkavaara et al., 2013; Suomalainen et al., 2014; Ristorto et al., 2015; de Oliveira et al., 2016; Yang et al., 2017; Barreto et al., 2019). Miniature multispectral cameras, such as MicaSense RedEdge and Altum (MicaSense, 2020a), and Tetracam Mini-MCA (Tetracam, 2020), have spread widely in drone usage, as they are often smaller and cheaper than true hyperspectral cameras. Miniaturized multi- and hyperspectral cameras are suitable for remote sensing drone applications, providing interesting and cost-effective techniques for accurate geometric and radiometric characterization of objects.

Generally, a fundamental requirement for quantitative remote sensing analysis is the utilization of accurate reflectance factor values. Cameras measure radiance and save it as digital numbers (DN), but these cannot be used directly in quantitative analysis as they are affected by illumination changes and sensor uniformities (Smith and Milton, 1999). Thus radiometric calibration of the camera is the prerequisite for accurate reflectance transformation. It normally involves dark current, flat field, spectral response, and absolute radiometric coefficients and allows the camera DNs to be converted to accurate at-sensor radiances (Aasen et al., 2018). Typically, remote sensing camera manufacturers provide camera calibration parameters that are estimated in laboratory conditions, but, especially as the device ages, they may differ from the correct values applicable in field use. For example, Mamaghani and Salvaggio (2019a) assessed the manufacturer's radiometric calibration of two MicaSense RedEdge cameras and observed that the difference in the overall radiance images came from the manufacturer's vignette and radiometric calibration coefficients, while dark current and relative spectral response curves fitted well to their calibration. Overall, their own calibration provided lower errors in radiance and reflectance values than using the manufacturer calibration.

The reflectance transformation of drone remote sensing images fundamentally requires determination of illumination conditions in the target area (Aasen et al., 2018). This can be achieved by: (1.) Simulating the irradiance using *atmospheric radiative transfer models* based on accurate knowledge of the atmosphere composition (Clark et al., 2010; Zarco-Tejada et al., 2012); (2.) using reflectance reference targets with known reflectance factors placed in a well-illuminated position in the surveyed area (Aasen et al., 2018); (3.) Having an on-ground static device to continuously measure the irradiance during the flight (Burkart et al., 2014); (4.) Having an on-board irradiance sensor (commonly also referred as incident light sensor ILS, or sunshine sensor). All of the above methods are working solutions in stable clear-sky conditions in open areas. Currently, spectral drone processing workflows are often based on indirect reflectance transformation utilizing reference reflectance panels installed in the interest area and applying the empirical line method (ELM, method 2) (Del Pozo et al., 2014). However, in partially cloudy conditions, the ground-reference methods (2&3) work only locally and determining the parameters for the atmospheric model (1) becomes infeasible. Also, the ground-reference methods work ideally when placed on open terrain and the ground-level irradiance on panels or irradiance sensor matches accurately the above-canopy irradiance. Consequently these methods have challenges in e.g. forested areas and in areas where the surrounding objects block direct and diffuse skylight and reflect additional light. In order to overcome the non-local variations outside the representative panel's area, some authors have proposed to use multiple panels placed on the site, so that each image contains at least one calibration panel, to transform the DN value into surface reflectance (Wang and Myint, 2015; Iqbal et al., 2018). The direct reflectance method (4), uses a radiometrically calibrated downward-looking camera and upward-looking irradiance sensor allowing the reflectance factor transformation of the images in real time without on-site reflectance reference panels. Thus, it has potential to be

effective in all of these conditions by always measuring the local irradiance. However, what is commonly overlooked, is that as the irradiance sensor reading is highly tilt sensitive. The irradiance sensor must be installed on top of the drone either on a stabilized gimbal or tilt-effects in data must be otherwise corrected.

An on-board upward-looking irradiance sensor allows for obtaining the transformation to reflectance factors directly even in real time during the flight. Direct reflectance capability for both real-time and post-processed solutions is of interest for remote sensing applications (Oliveira et al., 2018). Fast and reliable direct reflectance transformation using irradiance data collected for each image throughout the flight campaign is essential, especially, in unstable illumination conditions (Honkavaara et al., 2013; Hakala et al., 2018) and in challenging areas, such as forests (Nevalainen et al., 2017) and waters (Ortiz et al., 2017), where setting up properly illuminated reference panels for the ELM is not always feasible. Beyond-visible-line-of-sight (BVLOS) missions, that cover larger areas using drones, are becoming feasible in the near future. These missions would make the use of reference targets unsuitable in practical applications due to representing the illumination conditions only in a local area. Recently, point spectrometers attached to drone platforms have been used for measurements of reflectance of vegetation. Burkart et al. (2014) developed a drone spectrometer system based on a compact Ocean Optics STS spectroradiometer onboard the drone to measure the upwelling radiance, while another ground spectrometer acquires the irradiance over a white Spectralon panel. The air and ground systems are wirelessly synchronized for simultaneous white reference collection. The system was calibrated with corrections for dark current, stray light, spectral offset, and a cross-calibration using an ASD FieldSpec 4. This system was later applied as a flying goniometer to measure the bidirectional reflectance distribution function of vegetation (Burkart et al., 2015). However, point spectrometers data cannot be spatially separated in spectral pixels as in cameras, since each spectral measurement includes information from all objects within the FOV of the sensor (Aasen et al., 2018; Gautam et al., 2020). Multispectral cameras such as MicaSense RedEdge and Altum include an irradiance sensor (also called down-welling light sensor - DLS) and calibrated reflectance panel in order to accomplish the reflectance transformation (MicaSense, 2020a). With the Tetracam Micro-MCA, the sixth channel presents an irradiance sensor, called incident light sensor (ILS), which contains a band pass filter and an optical fiber (Tetracam, 2020). Jiang et al. (2019) assessed the Micro-MCA for monitoring winter wheat crops. They performed radiometric calibration on a Micro-MCA and compared the reflectance transformation using panels and ELM versus the direct reflectance using the camera irradiance sensor. Hakala et al. (2018) proposed a drone based remote sensing system for measuring the reflectance with a 2D frame format hyperspectral camera measuring the reflected radiance and a small Ocean Optics USB2000+ spectrometer (OO, Ocean Optics, Largo, FL, USA) integrated recording the down-welling irradiance. As the gimbal used to compensate for the tilting of the spectrometer optics did not give acceptable results, the authors utilized a ground based spectrometer for compensating the impacts of tilting of the sensor. Bendig et al. (2020) flew their AirSIF sensor, which uses an Ocean Optics QE Pro spectrometer and a multiplexer that allows it to alternate observing upwelling radiance and downwelling irradiance. As the cosine response of the irradiance probe was not accurate enough (Bendig et al., 2018), they developed a cross-calibration method where specific calibration coefficient between the upwelling and downwelling sensors are determined before flight using a Spectralon panel. Such coefficients are valid only for a short time, before illumination conditions or the solar zenith angle changes substantially, but the method can allow useful utilization of a low quality irradiance probe in short missions.

In drone remote sensing, the atmospheric effects are often neglected due to the low flight altitudes (Hernández-López et al., 2012; Iqbal et al., 2018). However, studies have indicated that atmospheric correction can be important for precise radiometric measurements also in drone-based

multispectral (Guo et al., 2019; Mamaghani and Salvaggio, 2019b) and thermal (Heinemann et al., 2020) images. The atmospheric effects can be corrected using atmospheric models or two-point ELM (Aasen et al., 2018).

The objective of this study was to develop and assess a drone-based workflow for direct reflectance processing and implement it on our hyperspectral remote sensing system. Firstly, we will present the direct reflectance workflow with a novel atmospheric correction method. Next, we describe the thorough radiometric calibration procedures required. In this study, the system consists of the hyperspectral camera (Senop Rikola HSI, model 2018) and the FGI Aerial Image Reference System (FGI AIRS), which measures irradiance spectra in real-time, RTK (real time kinematic) GNSS (global navigation satellite system) position, and the roll-pitch-yaw orientation for each camera exposure (Suomalainen et al., 2018). Finally, we present results of flight experiments and assess the accuracy of the reflectance factors produced using the proposed workflow.

2. Materials and methods

2.1. Direct reflectance workflow

In remote sensing data, the reflectance factor (R) of interest is usually the ratio between *at-target radiance* (L_{AT}) and *above-canopy irradiance* (E_{AC}):

$$R = \frac{\pi L_{AT}}{E_{AC}} \quad (1)$$

With a clear atmosphere and low flying altitude, it is a common practice to assume that the drone-based *at-sensor radiance* is equivalent to the *at-target radiance*. This can be a harmless assumption at low altitudes especially in cases where on-ground reflectance reference panels are used to determine the irradiance, as this introduces similar atmospheric biases to both irradiance and radiance measurements. However, such cancelation does not occur if the irradiance is measured by an onboard sensor, and thus the importance of atmospheric effects (Fig. 1) is greater in such applications.

For atmospheric correction in the direct reflectance workflow, we have developed a novel method that utilizes two reference panels of different reflectances. As visualized in the Fig. 1, the *at-sensor radiance* (L_{AS}) that the camera observes for the panels 1 and 2 are defined by equations:

$$\begin{cases} L_{AS1} = \frac{1}{\pi} \tau R_1 E_{AT} + L_{DIF} \\ L_{AS2} = \frac{1}{\pi} \tau R_2 E_{AT} + L_{DIF} \end{cases} \quad (2)$$

where τ is the *atmospheric transmittance* between the target and the camera, R_1 and R_2 are the reflectance factors of the panels, E_{AT} is the *at-target irradiance* hitting the panels, and L_{DIF} is the *diffuse radiance* component introduced by the atmosphere. If the panels are placed next to each other in a uniformly illuminated area on ground, it is fair to assume that the transmittance, irradiance, and diffuse radiance are equal for both panel observations. Unlike in the ELM approach, this assumption does not require the panels to receive the clean above-canopy irradiance, but they can be placed also e.g. in a narrow forest opening or even in a shadowed area, with the only requirement being that both panels are illuminated similarly. With these assumptions, even if the *at-target irradiance* is unknown, we can solve the diffuse radiance component for each camera spectral band:

$$L_{DIF} = \frac{R_1 L_{AS2} - R_2 L_{AS1}}{R_1 - R_2} \quad (3)$$

This equation allows determination of the diffuse radiance component, which is valid for atmospheric correction only in the same illumination conditions and at the same flight altitude as the imaging of the panels was done. To make the diffuse light correction usable in the whole mapping flight, we must handle two effects affecting the diffuse radiance. Firstly, if the illumination conditions change, due to e.g. clouds, the atmospheric diffuse radiance is expected to change also. Thus, instead of using the determined diffuse radiance in atmospheric correction, it is better to convert it to an atmosphere apparent reflectance (R_{ATM}), which should be more stable in varying illumination. Secondly, if the distance to the target (h) varies from the distance during panel calibration (h_{panel}), this will also affect the thickness and effect of the atmosphere. Ideally, as the sensor-target distance varies over the view directions within the image, the correction should be calculated pixel-wise. At the low altitudes, we can assume that the atmosphere under the drone flight area is homogenous and thus the L_{DIF} depends linearly on the sensor-target distance. With these two adjustments, we can generate an equation for *atmosphere apparent reflectance* (R_{ATM}):

$$R_{ATM} = \frac{h}{h_{panel}} \frac{\pi L_{DIF}}{E_{AS}} \quad (4)$$

Strictly speaking, this atmosphere apparent reflectance is valid only

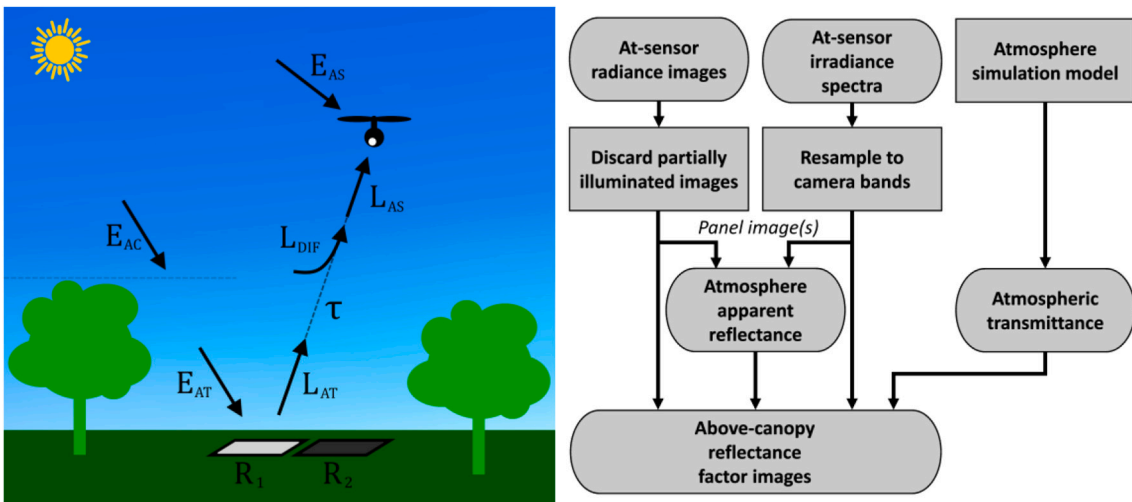


Fig. 1. (Left) Irradiance (E), radiance (L), reflectance factor (R), and transmittance (τ) concepts affecting the drone observation between at-target (AT), above-canopy (AC), and at-sensor (AS) positions. (Right) Flowchart of the direct reflectance workflow.

in the very same solar and view angle geometry and in the surroundings at which it was determined in. There can be multiple effects affecting it. Firstly, the radiance following sun-terrain-atmosphere-sensor path varies directly with reflectance of the surrounding terrain. Secondly, the anisotropic scattering in atmosphere causes that the sun-atmosphere-sensor component of the apparent reflectance should vary for camera pixels observing different view directions relative to sun. Thirdly, even in nadir view, the reflectance may not be perfectly stable when illumination geometry changes due to clouds. Taking these variations in R_{ATM} into account, could be a point of improvement for the atmospheric model, but for the sake of simplicity, we here make the assumption that the atmosphere apparent reflectance is constant for all pixels in varying illumination conditions.

If the at-target irradiance incident on the panels is unknown, it is not possible to solve for the atmospheric transmittance from this panel data. Thus, the transmittance must be determined using other methods, e.g. by atmospheric simulation. In this study, we simulated the atmospheric transmittance between target on the ground and the camera at 100 m above-ground-level (AGL) altitude using the 6S simulation (Vermeote et al., 1997) through the Py6S Python interface (Wilson, 2013). The simulation considered the “US Standard 1962” atmosphere model and “Urban” aerosol model, and it was repeated with two horizontal visibility values (23 km and 10 km). The two transmittances are the pre-calculated options that can be selected depending if the weather is perfectly clear or with slightly reduced visibility. The selected transmittance spectrum for 100 m altitude is then scaled to the actual sensor-target distance using the Beer-Lambert law:

$$\tau = (\tau_{100})^{\frac{d}{100}} \quad (5)$$

With the atmospheric transmittance and apparent reflectance determined, we can apply the atmospheric correction to the drone based observations:

$$E_{AC} = \tau E_{AS} \quad (6)$$

$$L_{AT} = \frac{1}{\tau} \left(L_{AS} - \frac{1}{\pi} R_{ATM} E_{AS} \right) \quad (7)$$

By inserting these to the Eq. 1, we get the equation for producing atmospheric corrected above canopy reflectance factors from drone based observations:

$$R = \frac{1}{\tau^2} \left(\frac{\pi L_{AS}}{E_{AS}} - R_{ATM} \right) \quad (8)$$

Although, the workflow utilizes on-ground reference panels for determining the atmospheric correction parameters, it can still be used in real-time direct reflectance processing. Unlike the ELM correction parameters, our parameters are mathematically defined in such a way that they are not directly dependent on absolute level of irradiance and thus they may be assumed to be relatively stable even in changing illumination. Also as a practical point, these parameters can be determined before the main flight or values from earlier flight in similar

conditions may be reused, allowing real time processing of the data.

2.2. Remote sensing equipment

In this study, we used a hyperspectral frame camera (Fig. 2a) based on the Fabry-Perot interferometer (FPI) technology and manufactured by Senop Ltd., Oulu, Finland, (model *Rikola HSI 2018*). The adjustable FPI filter allows users to select the spectral bands of the hyperspectral cubes according to the requirements of the application (Mäkynen et al., 2011). The FPI filter itself is not able to separate multiples of wavelength, and thus the camera has a beam splitter and two monochrome CMOS sensors (de Oliveira et al., 2016), of which one is configured to record the visible bands (500–636 nm) and the other the VNIR/NIR bands (650–900 nm). The nominal focal length is 9 mm and image size is 1010×1010 pixels with pixel size of $5.5 \mu\text{m}$. The camera was set to collect 46 bands within the 504–908 nm range with spectral resolutions ranging between 3 and 10 nm (full width at half maximum, FWHM). Like most cameras without thermal-stabilization, the dark current in images varies with the system temperature. To counter this effect, in all of the experiments described in this paper, the camera has been turned on and its temperature has been allowed to stabilize at least 15 min before a dark current datacube is collected and the useful data is acquired. A monochromator setup was used to determine the spectral response curves for each band (Pekkala et al., 2019). The central wavelengths and FWHMs determined from these are shown in Table 1. The camera acquires the spectral bands by scanning over a sequence FPI filter bandpass wavelengths. With 46 bands, this scan takes typically 1.1 s to finish and a new scan can be started at 2 s intervals. If the camera platform is moving, each spectral band in the same cube is acquired at different position and attitude (Honkavaara et al., 2017).

The FGI AIRS (Fig. 2b) is a sensor unit for drones that can provide the irradiance spectrum, Real Time Kinematic (RTK)/Post Processed Kinematic (PPK) GNSS position, and orientation for each frame acquired by the attached camera(s). For irradiance measurement, the FGI AIRS uses an Ocean Optics USB2000+ spectrometer (350–1000 nm, FWHM < 1 nm) equipped with diffuser optics with cosine response. Furthermore, to provide reliable irradiances on tilting drone platforms, the AIRS utilizes a novel tilt correction method based on three extra photodiode irradiance sensors, that lay tilted 10° to opposite directions. The system hardware and processing methods are described in detail in (Suomalainen et al., 2018). In this study, we present the cosine response calibration and improvements made to the AIRS cosine collector optics, which improve the absolute accuracy of the AIRS irradiances in varying illumination conditions.

A custom quadcopter drone (Fig. 2c) was utilized to carry the sensor payloads and to collect the remote sensing data. The drone has a payload capacity of 4 kg and flight time of 20 min with 2 kg payload. The hyperspectral camera and an RGB camera Sony A7R (Sony Corporation, Minato, Tokyo, Japan) were installed on a vibration suppressed mount under the drone pointing straight down. The AIRS was attached on the very top of the drone frame, to avoid obstructions in the hemispherical

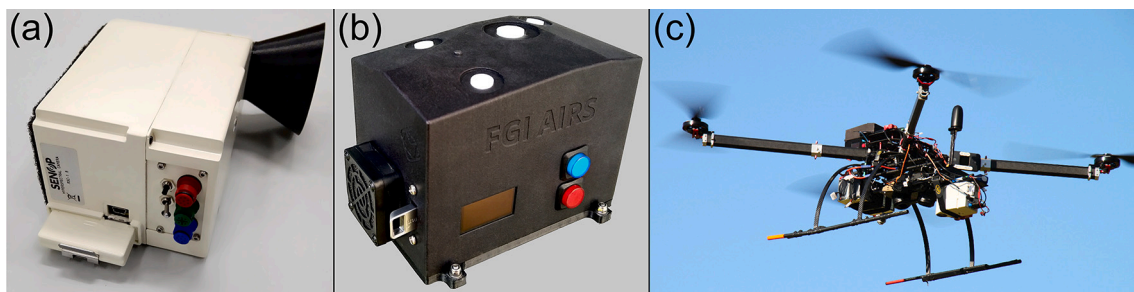


Fig. 2. (a) The Senop Rikola hyperspectral camera, (b) the Finnish Geospatial Research Institute Aerial Image Reference System (FGI AIRS), and (c) the custom drone with the sensors onboard. The black cone on the Rikola camera is a custom addition to help reduce stray light issues found in the camera optics.

Table 1

Hyperspectral camera bands. The center wavelength and spectral resolution (FWHM) for each of the 46 bands. Units as nanometers.

Center	FWHM	Center	FWHM	Center	FWHM	Center	FWHM	Center	FWHM
504.28	6.36	593.37	6.18	684.56	6.66	773.71	4.30	863.54	9.46
512.91	7.26	601.40	6.49	693.97	6.82	782.85	5.95	873.07	9.21
521.48	7.47	611.64	7.64	701.60	5.01	792.18	5.80	881.51	9.55
530.75	6.75	620.27	8.30	711.43	4.43	800.88	6.46	890.21	9.03
539.46	7.42	628.86	7.05	720.08	4.97	809.82	5.67	899.16	9.58
548.45	6.64	643.80	6.76	728.95	3.92	818.49	6.62	908.17	8.90
557.59	7.35	648.67	6.58	738.01	4.86	828.84	9.05		
566.28	6.47	657.82	7.58	746.76	4.11	837.57	10.16		
575.31	7.02	666.88	6.72	756.03	4.49	846.22	9.24		
583.98	6.60	676.21	7.52	764.56	3.67	855.44	9.93		

fields-of-view of the irradiance sensors. The hyperspectral camera and the AIRS were connected with a trigger cable to allow synchronization of the devices.

2.3. Irradiance sensor cosine response and absolute radiometric calibrations

A prerequisite for any accurate irradiance measurement in varying illumination conditions is to ensure that the cosine response of the optics utilized is correct. The proper cosine response ensures that the sensor outputs the correct irradiance reading independent of the solar zenith angle and the cloud cover.

In this study, the irradiance is measured onboard using the AIRS and the on-ground reference measurements are performed using an ASD FieldSpec 4 (Malvern Panalytical Ltd., Malvern, United Kingdom) with its Remote Cosine Receptors (RCR) irradiance probe. Thus, to measure cosine response of AIRS and ASD FieldSpec irradiance optics, we set up a laboratory test setup (Fig. 3) consisting of a rotator holding the irradiance sensor, a homogenous beam of light, and a black box that minimizes the amount of diffuse light. The irradiance probe was installed on a motorized rotator so that the axis of rotation went accurately through the optical center of the irradiance probe with geometric stability in order of one millimeter. The incident light was produced using a 1000 W power-stabilized QTH light bulb (Oriol 66886 and 69935, Newport Corporation, Irvine, CA, USA) placed at approximately 2-m distance from the point of measurement with no collimating optics but only an aperture to restrict a narrow beam of light. A collimated beam would introduce smaller r^2 falloff errors than the uncollimated beam, but with

our lamp and optics the collimated beam showed clear inhomogeneity reproducing the shapes of the lamp filament. The r^2 error in measurement is affected by instability of the physical center of the cosine optics due to imperfectly centered axis of rotation ($\sim \pm 1$ mm) and on the large illumination zenith angles by the possible shift of the effective optical center towards the more illuminated front edge of the diffuser. For the diffusers with 7.5 mm radius, the shift was estimated to be approximately in order of 1 mm. With the lamp at 2-m distance, each millimeter of offset in distance causes 0.1% error in measurement. With the given numbers, the r^2 errors from an uncollimated beam were estimated to be smaller than the errors from inhomogeneous collimated beam. To minimize diffuse light disturbing the measurement, the sensor was placed in a box that was internally covered with spectrally black canvas with reflectance of approximately 0.05. The light beam was let in through an aperture ($d = \sim 10$ cm) to interact with the sensor. The non-intercepted part of the beam was let out through a slightly bigger aperture on the opposite side and later absorbed to a black canvas placed about 1 m away.

To measure the sensor's cosine response at all light incident angles, the irradiance probe was rotated through a range of $\pm 95^\circ$ from the direction of the beam while measuring sensor irradiance reading. With the ASD FieldSpec, the rotator was stopped every 5 degrees where a spectrum measurement was taken and the angle of rotation was recorded manually. With AIRS, the measurements were taken during slow continuous rotation, sampling a spectrum at approximately 2° intervals, and the angles were recorded by the AIRS internal inclinometer.

This setup was used to first characterize the cosine responses of the original ASD FieldSpec irradiance probe and the FGI AIRS 2018 irradiance optics. As the cosine accuracies of all original optics were found to be insufficient, the measurement system was then used to test a series of modified ASD and AIRS optics to find probe geometries with near-ideal cosine responses.

The geometries of both the ASD probe and modified AIRS optics follow the basic shadow ring geometry as shown in Fig. 4. With the ASD probe, the modifications to the original were kept at minimum and only the depth of the shadow ring was reduced by inserting 3D printed black rings of varying thickness around the base of the diffuser. Such modification reduces the response significantly at non-nadir illumination angles, but should have no significant effect in nadir illumination as the vertical edges of the diffuser are parallel to the light incidence angle and are surrounded by only black surface. Thus the edges are effectively not externally illuminated and the addition of a black ring has almost no effect to light reaching the sensor behind the diffuser. As the calibration of the ASD irradiance probe has originally been performed in nadir illumination, this meant that the modification did not affect its absolute calibration coefficients, but simply improved its accuracy on higher illumination zenith angles. In the optimization of the AIRS irradiance spectrometer and photodiode optics, all of the geometry parameters shown in Fig. 4 were adjusted. The shadow ring and the frame of the optics were 3D printed of black plastic. The diffusers were cut from a white PTFE pad and sanded to desired thickness.

The new FGI AIRS irradiance optics were given an absolute

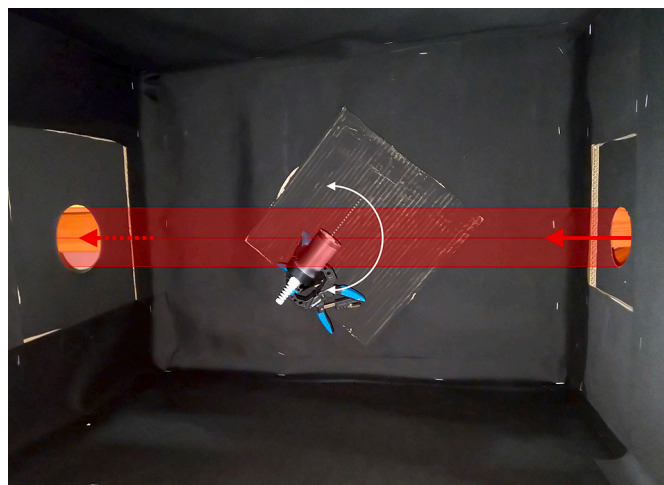


Fig. 3. The ASD FieldSpec irradiance probe inside the cosine response measurement setup. A homogenous beam of light enters the box from the opening on right illuminating the irradiance probe in the center. The probe is rotated through angles $\pm 95^\circ$ from the beam direction to record irradiance readings at all light incident angles.

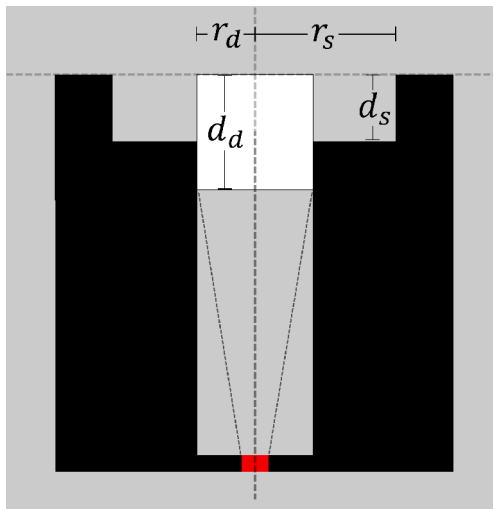


Fig. 4. Basic geometry of a shadow ring based cosine collector/irradiance optics. By adjusting the radiuses and thicknesses of the PTFE diffuser (r_d and d_d) and the shadow ring (r_s and d_s), it is possible to design an irradiance probe with near-ideal cosine response.

irradiance calibration by transferring the absolute calibration of the ASD FieldSpec irradiance probe to it. This was done by using the cosine response measurement setup described above. First, the ASD irradiance probe was placed in a well-determined position inside the black box pointing directly towards the light source (“nadir illumination geometry”) and a reference irradiance spectrum was measured. Next, the ASD probe was removed and AIRS sensor was placed in the same position and orientation to measure raw irradiance spectrum. Pseudo-irradiance spectrum was calculated by removing dark current from the raw irradiance spectrum and dividing the result with integration time. The new absolute irradiance calibration coefficient was determined as ratio of these two spectra.

2.4. Hyperspectral camera radiance calibration

The original radiometric calibration of the hyperspectral camera was found to have several non-idealities in the camera performance. Initial tests on the camera had revealed issues where the actual exposure time was apparently not matching the nominal exposure time and where imperfections in optics caused stray light issues in the image. To correct for these problems and to produce accurate absolute radiance images, we performed a series of calibration measurements and developed our own processing chain.

The basic equation to convert the raw pixel digital numbers on band k to radiances (L_{ijk}) is:

$$L_{ijk} = c_k \frac{DN_{ij} - DC_{ij}}{f_{ijk} t_{int}} \quad (9)$$

where DN_{ij} is the raw digital number in pixel $[i, j]$, DC_{ij} is pixelwise dark current count, f_{ijk} is the flat field image, t_{int} is the integration time of the camera, and c_k is the bandwise absolute calibration coefficient.

The flat-field calibration is described in detail in Kokka et al. (2019), but we give here also a short description of the process. The method consisted of scanning the field of view (FOV) of the camera with a broadband radiance source from an integrating sphere that covered the FOV only partially at the focus distance and combining the captured data cubes to produce a uniform radiance source filling the whole FOV. The camera was installed onto a two-axis rotary stage at 1 m distance from the aperture of the integrating sphere. The whole setup was enclosed in a black cabinet with two apertures to reduce stray light in the FOV of the camera. The measurements were done with a 1.2°

rotation step size in both axes. The collected data was merged into a single data cube by removing the dark signal, removing pixel areas not irradiated directly by the source and the edges of the irradiated area in the images, and filtering high-frequency components. The flat-field correction matrix (f_{ijk}) was computed by convolving each spectral band with a Gaussian filter kernel. The flat-field calibration method obtained an average standard deviation of 0.40%.

When testing the camera on different exposure times, we found out that Eq. 9 failed to produce constant radiances while only camera integration time was varied. Thus we had to apply a correction:

$$t_{int} = t_{nominal} + \Delta t \quad (10)$$

where $t_{nominal}$ is the nominal exposure time set to the camera and Δt is calibration parameter for integration time offset.

To determine the integration time offset, we set up a laboratory calibration experiment. The p50 panel was set standing up and illuminated perpendicularly using the stabilized QTH light bulb from approximately 1.5 m distance. The hyperspectral camera and ASD FieldSpec spectrometer with 18° optics were installed on a static tripod, placed next to the beam of light at approximately 50 cm distance from the panel, and pointed at the center of the illuminated area. Then, hyperspectral camera images were acquired using nominal exposure times of 8 ms, 12 ms, 18 ms, 24 ms, and 30 ms. To validate stability of the illumination, for each hyperspectral image, a reference radiance spectrum was measured using the ASD FieldSpec. The integration time offset was then determined by minimizing the variation in processed camera radiances.

The camera was also found to suffer from stray light and it was necessary to correct for these. The stray light issues in the camera are most likely caused by imperfections in the camera optics, which scatter light to the wrong parts of the sensor. To correct for stray light inside the camera, we determined a correction that follows an equation:

$$L'_{ijk} = L_{ijk} - s_k \widehat{L}_k \quad (11)$$

where L'_{ijk} is the stray light corrected at-sensor radiance, \widehat{L}_k is average radiance in the uncorrected image, and s_k is the stray light calibration coefficient. This correction assumes that the average image intensity acts as good proxy for amount of diffusing light entering the camera optics. To block the diffuse light entering the lens from outside the camera field of view, we installed a black cone on the camera main lens (Fig. 2a) that blocks most of the light hitting the lens from outside FOV.

The stray light calibration coefficient was determined in the laboratory by taking images of constant targets in front of varying backgrounds. Similar method has been proposed by Rykowski and Kreysar (2005). This was done by installing small black and white reflectance targets on a holder and illuminating them with the stabilized QTH light source. The camera was installed on a static tripod and pointed at the targets. Then the camera was used to acquire images of the targets (see Fig. 10) with black and white panels in the background. The s_k was then linearly solved by assuming that the radiance of small targets should remain constant in images with different backgrounds.

As the final calibration step, the absolute radiometric calibration (c_k in Eq. 9) was determined in flight using AIRS irradiances and reflectance reference panels. The camera could also have been calibrated in a laboratory using more traceable ASD FieldSpec calibration, but by performing the calibration in conditions resembling real use maximizes the accuracy of direct reflectance factors produced with the camera+AIRS combination. The calibration data was acquired by hovering the drone with the hyperspectral camera and the FGI AIRS above the four reference panels (p50, p25, p10, p05) at 6 to 16 m altitude. The hyperspectral raw images were converted to *pseudo at-sensor radiances* using a bandwise absolute calibration coefficient set to one ($c_k = 1$ in Eq. 9). The pseudo at-sensor radiances recorded by the camera for each panel were manually extracted from images. The respective panel reference

radiances were calculated using the AIRS irradiances and known reflectance factors of the panels. Using the p50 panel data, the ratio of the pseudo at-sensor radiance and the reference radiance was then determined to be the true value for c_k . The radiances of the remaining panels were used for validation.

2.5. Field experiment

The experimental flights using the FGI drone and sensors were conducted over the permanent calibration test field (Fig. 5) located in Sjäokulla (60.242 N, 24.383 E), southern Finland (Honkavaara et al., 2008). Altogether three permanent ground control points (GCPs) around the test field were surveyed using a Topcon Hiper HR RTK GNSS receiver (Topcon, Tokyo, Japan) with 6.4 mm horizontal and 12.24 mm vertical accuracy based on Topcon's reported positioning performance (Topcon, 2016). The average altitude of the site is 40 m above sea level. The flight campaign was carried out on 20 August 2019, between 13:30 and 14:30 local time (UTC + 3 h). Over the course of the flights, the solar zenith angle changed from 47.8° to 48.8°.

For collecting validation data, four high-quality calibration panels were used. The panels, 1 m × 1 m in size and with nominal reflectances equal to 50%, 25%, 10%, and 5% (referred, respectively, p50, p25, p10, and p05), were placed on a balanced stand approximately 1 m above the ground. These panels have been built in-house by installing Zenith Polymer films (SphereOptics GmbH, Uhlidingen, Germany) on flat aluminum honeycomb panels (6 mm Potmacore panels by Potma, Pello, Finland). Additionally, two panels with nominal reflectances of 50% ("GP", matte paint on panel) and 3% ("BC", carpet on panel) were placed directly on ground and used for independent atmospheric calibration. With both panel types, the panels' nadir-view reflectance factors vary slightly with illumination direction and the nominal reflectances are not accurate enough to be used as the true reflectance factor. Thus, the ASD FieldSpec spectrometer and a white reference Spectralon panel (Lab-sphere, Inc., North Sutton, NH, USA) were used to measure the nadir reflectance factor of each reference panel by averaging 10 measurements.

In the first experiment, we performed an elevator flight rising from 10 m to 150 m AGL altitude acquiring hyperspectral datacubes and RGB images at 2.6 m intervals on average (Fig. 5). The purpose of the elevator flight was to assess the workflow and atmospheric effects at different altitudes. In the second experiment, two mapping flights consisting of four parallel flight lines at 100 m AGL altitude were flown repeatedly over the test field area and panels to evaluate stability of AIRS irradiance measurement and acquired reflectance factors in normal mapping use

case. The ASD FieldSpec with the improved RCR was installed on a tripod next to the panels to record on-ground reference irradiances.

During the campaign, the sky was mostly blue with approximately 1/8th of the sky covered by fast-moving low altitude cumulus clouds. The elevator flight and the first mapping flight were performed during a fully clear period without significant cloud shadows in the test area. The second mapping flight contained data in both clear and cloud shadowed illuminations.

Since the bands and spectral resolutions of the camera and irradiance sensors were different from each other, spectral resampling was needed to fuse the data. The hyperspectral camera was configured to acquire 46 spectral bands as described in Table 1, while the ASD FieldSpec has a spectral resolution of 3.5 nm at the wavelengths of below 1000 nm, and the AIRS irradiance spectra have a resolution of 1 nm at the range of 350 nm to 1000 nm. Thus, the ASD reference reflectance spectra and AIRS irradiance spectra were resampled to match the spectral responses of the hyperspectral camera bands by taking a weighted average using each band's measured spectral response spectrum as weights.

As the bands of the hyperspectral images acquired by Rikola camera are not aligned when the camera is moving, we estimated the position and orientations of each band of each data cube and corrected them by the relief displacement in an orthorectification process. This geometric processing followed a similar processing workflow as introduced by Honkavaara et al. (2017). First, exterior orientations of four key hyperspectral bands were determined simultaneously using AgiSoft Metashape Pro (v1.5; AgiSoft LLC, St. Petersburg, Russia) software. The photogrammetric image orientation process was performed to the RGB image data as well, in order to generate an accurate digital surface model of the area, which was used for the hyperspectral data orthorectification. The image orientations were estimated using the "Align" method with "High" quality. The camera geometric calibration was performed simultaneously during the image orientation process (self-calibration). Altogether three GCPs were measured manually.

Once the four bands of the data cubes were aligned in the Metashape, the in-house radBA software was used to orthorectify the image datasets following the process described in detail by Honkavaara et al., 2017. Firstly, the bands without orientations were matched to the aligned bands utilizing the sparse point cloud and exterior orientations were calculated using the space resection method. Next, to generate orthorectified images with reflectance values, the synchronized AIRS irradiance values for each band of the cubes were inserted in radBA. Finally, the images were orthorectified in radBA using the most-nadir method by taking the heights for each pixel from the Metashape DSM and the exterior and interior orientation parameters from the photogrammetric



Fig. 5. (Left) An aerial image of the Sjäokulla test site with a zoomed in view of the reflectance reference panels. (Right) The GPS flight paths and image positions from the elevator flight (red circles) and a mapping flight (blue crosses) above the reference panels. (For interpretation of the references to colour in this figure legend, the reader is referred to the web version of this article.)

processing. With the elevator experiment data, each frame was orthorectified separately. With the mapping experiment data, the fully sunny and fully cloudy images were selected manually and an orthomosaic was calculated for each dataset.

For the atmospheric correction of the elevator flight, we selected four data cubes acquired at approximately 100 m altitude. The average at-sensor radiance spectrum in the center 7×7 pixels was extracted for BC and GP reference panels. At 100 m altitude the Rikola GSD is 7 cm, which left 3 pixels wide buffer between the sampled area and edge of the panel to minimize the adjacency effects. The atmosphere apparent reflectance for 100 m altitude was then determined by applying these at-sensor radiances, the concurrent AIRS irradiance, and in-situ ASD FieldSpec panel reflectance factors to Eqs. 3 and 4. As the atmospheric transmittance we used the 23-km visibility simulation data, which was scaled separately for each image altitude. These coefficient spectra were then resampled using the spectral response functions of the 46 hyperspectral camera bands to produce bandwise atmospheric correction coefficients. The atmospheric correction of each mapping flight was done similarly to the elevator flight. One image of the each respective block (sunny and cloudy) was selected to extract the radiance spectrum of BC and GP panels and to compute the atmospheric correction for each orthomosaic.

To assess the accuracy of the radiometric calibration, the hyperspectral images from the elevator flight were transformed to reflectance factor data cubes with and without atmospheric correction. The reflectance factors of the high-quality reference panel were extracted from each orthorectified data cube using similar 7×7 sampling methodology as described above in atmospheric correction. At lower than 100 m flight altitudes this allowed keeping safe adjacency effect buffers of over 3-pixels between the sampled area and edge of the panel, but at higher altitudes this buffer size dropped to marginally acceptable 1.5 pixels. By comparing these remote-sensing reflectance factors to the reference values measured in situ using the ASD FieldSpec, we computed the mean, root mean square error (RMSE), and normalized root mean square error (NRMSE) of the differences.

To calculate ELM reflectance factors and to evaluate their accuracy, 6 images from the sunny period of the mapping flight were selected. These 6 images observed the panels p05–p50 from near nadir angle and, in mapping use, any one of them could have been picked for determining the ELM parameters. The Rikola at-sensor radiances for each panel were extracted from the images using the same 7×7 sampling methodology

as described above. An average of the 6 spectra was taken to form mean panel radiances. The mean panel radiances of p05 and p50 and ASD FieldSpec in-situ reflectance factors, were used to calculate the parameters of a two-point ELM. The ELM was then used to transform the p10 and p25 radiances from each image to reflectance factors.

3. Results

3.1. Cosine responses

The cosine responses of the ASD irradiance probe and the 2018 AIRS irradiance optics were found to differ significantly from the ideal. The results are shown in Fig. 6 and Table 2. Besides the accuracy of the sensor for specific solar zenith angles, the accuracy in isotropic illumination is also an important quantity, as it is an estimation of accuracy outdoors under cloud cover. If the isotropic and directional signed systematic errors, as presented in Table 2, differ significantly from each other, the irradiance sensor will experience non-linearity in events when the sun emerges from or goes behind the clouds. Such error is troublesome in both direct reflectance- and ELM-based transformations, as the main purpose of the irradiance sensor is to correct the data over such events.

Although the ASD FieldSpec spectrometer family has the reputation of being high-quality reference instruments, its irradiance probe in original form had unexpectedly the worst cosine response of all measured optics. Our data shows that due to non-ideal cosine response, the ASD probe overestimates irradiance by +6.4% in isotropic illumination (approximating cloudy conditions) and by +12.9% in directional illumination at 55° zenith angle. The 2018 AIRS spectrometer and photodiode irradiance optics, which were simple diffusers without shadow rings, also performed poorly. In isotropic illumination, the original spectrometer and photodiode optics underestimated the irradiance by -6.0% and -4.3% , respectively, and in directional illumination they were giving reasonably accurate readings only up to 50° or 60° illumination zenith angles.

To improve the irradiance accuracy, the ASD probe was modified. The main problem with the original ASD probe was that the sensor received too much light in the middle zenith angles (Fig. 6). This was corrected by adding a 3D printed black ring at the base of the diffuser, which reduced the height of the diffuser edge exposed to light (Fig. 7). Such a modification has no significant effect in nadir illumination angle,

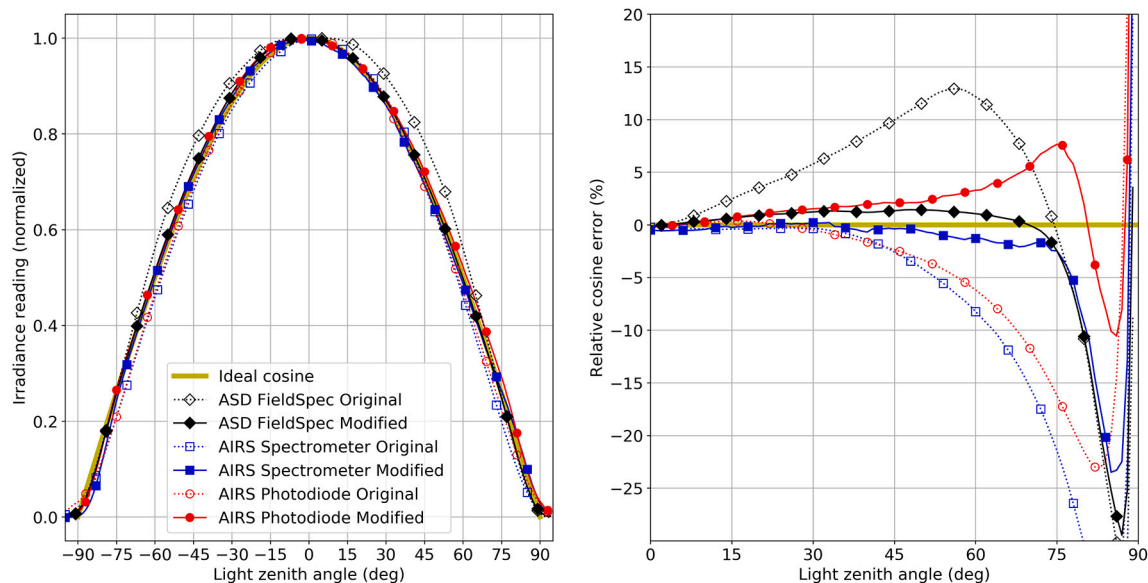


Fig. 6. (Left) The cosine responses of the AIRS and ASD FieldSpec RCR irradiance optics, before and after modification. Data is shown as average of spectral range 400–800 nm, but there were no significant variations between wavelengths. (Right) Same data, but shown as relative deviation from ideal cosine.

Table 2

Irradiance systematic errors in different illumination geometries due to non-ideal cosine response, assuming the irradiance sensor is absolutely calibrated in nadir geometry. Geometries with systematic errors larger than 2.5% and 5% are highlighted in yellow and red.

		Isotropic	Direct illumination zenith angle							
			10°	20°	30°	40°	50°	60°	70°	80°
ASD FieldSpec	Original	+6.4%	+1.3%	+3.5%	+5.8%	+8.5%	+11.5%	+12.2%	+5.9%	-10.8%
	Modified	+0.1%	+0.4%	+0.9%	+1.2%	+1.2%	+1.4%	+1.1%	-0.1%	-10.6%
AIRS Spectrometer	Original	-6.0%	-0.4%	-0.4%	-0.4%	-1.4%	-4.1%	-8.2%	-15.4%	-30.3%
	Modified	-1.3%	-0.4%	-0.2%	+0.2%	-0.7%	-0.6%	-1.3%	-1.9%	-9.3%
AIRS Photodiode	Original	-4.3%	+0.2%	+0.3%	-0.5%	-1.7%	-3.3%	-6.2%	-11.7%	-21.5%
	Modified	+2.3%	+0.3%	+1.0%	+1.5%	+1.9%	+2.1%	+3.3%	+5.6%	+1.9%



Fig. 7. (Left) The ASD FieldSpec RCR irradiance probe with the modification ring installed around the base of the diffuser. (Right) The improved FGI AIRS spectrometer and photodiode optics.

where the edges receive no direct illumination, or in very high illumination zenith angles where the covered area is anyway in the shadow of the shadow ring. By iteration, we found that the best cosine response was produced with shadow ring depth (d_d in Fig. 4) of 1.9 mm instead of the original 4.75 mm. With this modification the systematic errors due to non-ideal cosine response were reduced to only +0.1% in isotropic illumination and errors in the directional illumination remained within $\pm 1.5\%$ up to 70° illumination zenith angle.

The AIRS spectrometer and photodiode optics were redesigned using the shadow ring design. Through trial-and-error and many cosine response measurements, the optimum geometric parameters for the AIRS spectrometer were found to be [$r_d = 7.5$ mm, $d_d = 4.0$ mm, $r_s = 16.0$ mm, $d_s = 2.0$ mm] (Fig. 7). With the new spectrometer optics the systematic errors due to non-ideal cosine response, were reduced to only -1.3% in isotropic illumination and errors in the directional illumination remained within $\pm 1.9\%$ for illumination zenith angle up to 70°. For the AIRS photodiode optics, the optimum geometry was [$r_d = 5$ mm, $d_d = 3.0$ mm, $r_s = 10.25$ mm, $d_s = 1.28$ mm] (Fig. 7). With this shape the photodiode systematic errors were reduced to +2.3% in isotropic illumination and errors in the directional illumination were within $\pm 2.5\%$ for up to 55° illumination zenith angle. Although these accuracies are worse than other improved optics, they do not directly translate to AIRS irradiance errors, as the photodiodes in AIRS are not used for absolute irradiance, but only their relative values are used in the tilt correction.

3.2. Assessment of AIRS irradiance

The AIRS irradiance data was assessed using the Sjökkulla mapping flight data. The onboard AIRS irradiances had small deviations from the ASD FieldSpec irradiances measured on ground that are mostly linked to tilting and rotations of the UAV (Fig. 8). Using the ASD FieldSpec values as reference, the AIRS irradiance had NRMSE of 1.26% during a fully sunny period in the first mapping flight and 1.89% during the fully cloudy period in the second flight. During the sunny period, the ASD irradiance remained all the time between -0.8% and + 0.8% of the period mean, while during the cloudy period they varied within -2.6% and + 4.1% of the mean.

3.3. Hyperspectral camera calibration

The calibration measurement for determining the camera integration time offset parameter (Eq. 10) was implemented in the laboratory. The radiance spectra acquired using the hyperspectral camera of an illuminated panel showed large variations when measured with different nominal integration times when processed using manufacturer’s radiance processing (Fig. 9). An ASD FieldSpec reference measurements confirmed the stability of the illumination was better than $\pm 0.7\%$ during the whole experiment. By minimizing the variation in the processed radiance spectra, we determined the optimum value of the integration time offset to be -0.20 ms. By applying the integration time correction and dark current correction using black frames acquired for each exposure time, the effect of exposure time was effectively removed.

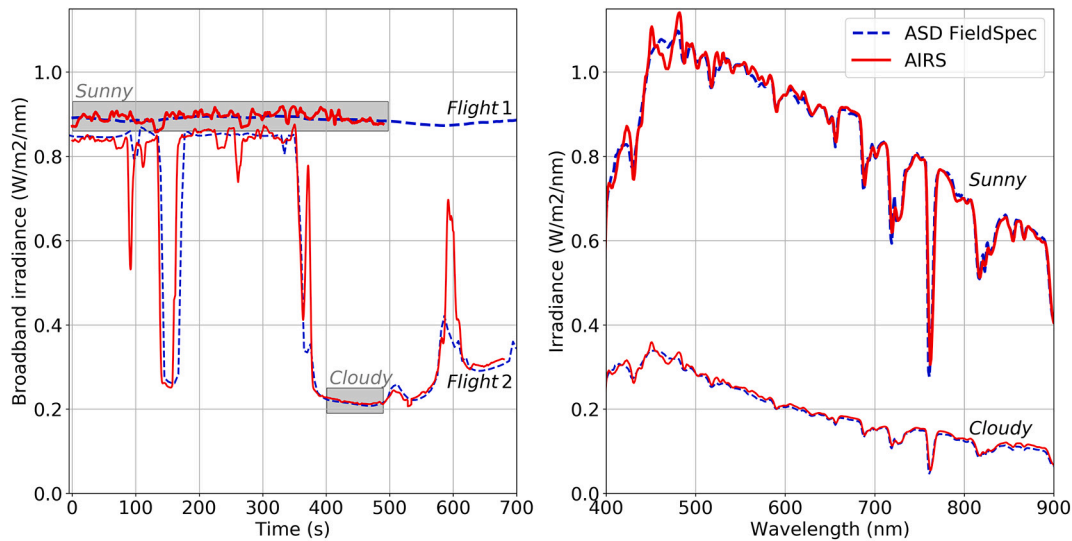


Fig. 8. (Left) Time series of broadband irradiance (400–900 nm) during the mapping flights as measured on ground using the ASD FieldSpec and onboard using the AIRS. (Right) Average irradiance spectra during stable illumination periods in the mapping flights. For easier comparison, the spectral resolution of the AIRS data has been reduced to 3.5 nm FWHM to match the ASD FieldSpec resolution.

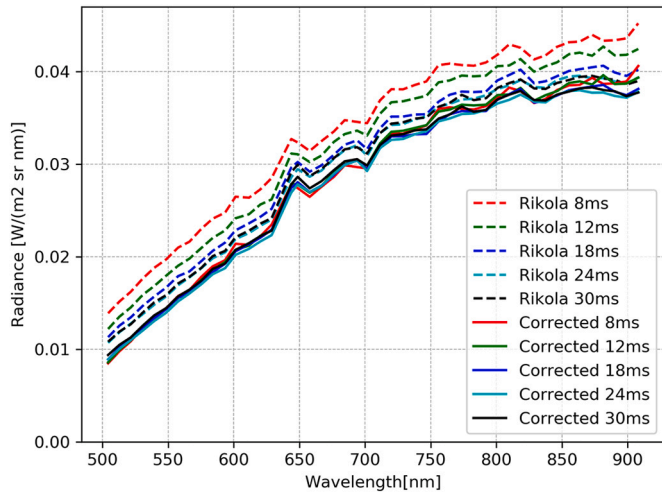


Fig. 9. Radiance spectra of a gray panel in stable illumination measured using the Rikola camera. The nominal exposure time of the Rikola camera was set to a range of value in 8–30 ms, which should not affect the measured radiances, but with manufacturer’s calibration and processing method it does. With dark current and integration time corrections, the effect of exposure time was effectively removed.

The camera stray light calibration measurement showed clear differences in the target radiances measured against dark and light backgrounds (Fig. 10). The stray light coefficient was then solved using the radiances of the dark target and whole image average radiances in the images with light and dark backgrounds. The coefficient spectrum is shown in Fig. 11.

3.4. Assessment of direct reflectance workflow

As a conventional method, the ELM was used to determine the reflectance factors of the panels during the sunny period in the mapping flight and, thus, to verify the compatibility of our direct reflectance workflow. The Fig. 12 left shows the radiances picked from the panels in 6 images that observed the panels almost straight down. If a single image was used instead of average of six, this would have caused uncertainty to the ELM parameters. When comparing the 6 images, the p50 average VIS

radiance had standard deviation of 1.0%, while in NIR the standard deviation was 0.5%. For the p05, the standard deviations were 1.8% in VIS and 5.2% in NIR. The Fig. 12 right shows the panel ELM reflectance factors in the 6 images. The ELM reflectance factors of the p25 showed NRMSEs of $\pm 2.0\%$ in VIS and $\pm 3.9\%$ in NIR relative to the ASD FieldSpec measurement. For the p10 ELM reflectances, the NRMSEs were $\pm 2.7\%$ in VIS and $\pm 4.8\%$ in NIR.

The proposed direct reflectance workflow was used to calibrate the image data acquired in the Sjöckulla test field and assessed using the spectrometer reference data. Initially, the atmospheric correction was not applied to the calibration. Fig. 13 compares the ASD FieldSpec reflectance factors of the four high-quality reference panels with the reflectance values of the same targets averaged from nine images acquired below 30 m altitude using our calibration method without the atmospheric correction. The low-altitude images allow assessment of system calibration without significant influence of atmospheric errors. Visually, all panels seem to fit well with the reference data in most of the bands. The p50 panel had relative errors (NRMSE) of $\pm 2.00\%$ and absolute errors (RMSE) of ± 0.009 , in VIS bands, and $\pm 1.75\%$ and ± 0.008 , respectively, in NIR bands. Similarly the p25 had the NRMSE and RMSE of $[\pm 1.16\%, \pm 0.0023]$ in VIS, and $[\pm 1.96\%, \pm 0.004]$ in NIR, while the p10 had $[\pm 2.28\%, \pm 0.0022]$ in VIS, and $[\pm 1.81\%, \pm 0.0018]$ in NIR, and the p05 had $[\pm 3.56\%, \pm 0.0024]$ in VIS, and $[\pm 2.69\%, \pm 0.0018]$ in NIR.

In order to assess atmospheric effects and accuracy of the proposed atmospheric correction at different altitudes, the images from the fully sunny elevator flight were processed to reflectance factors with and without the atmospheric correction. The reflectance factors of the reference targets were compared to the spectrometer reference values. Without atmospheric correction, the relative error increased with the increasing flight height, especially on the dark panels (Fig. 14). Images acquired at 50 m AGL presented relative differences higher than 5%, and the errors got worse the higher the altitude. The atmospheric correction significantly improved the effects on the dark panels, improving their accuracy to better than 5% level on all tested altitudes, but had only little effect on the bright panels (Fig. 14).

The spectral effects of the altitude and atmospheric correction can be observed in Fig. 15, which presents the mean reflectance factors of the p05 and p50 panels from four images acquired at different flight altitudes (5–20 m, 45–55 m, 95–105 m, and 145–155 m). After the atmospheric correction, the reflectance factors of p05 became more similar for each altitude, while p50 had the opposite effect, deviating slightly

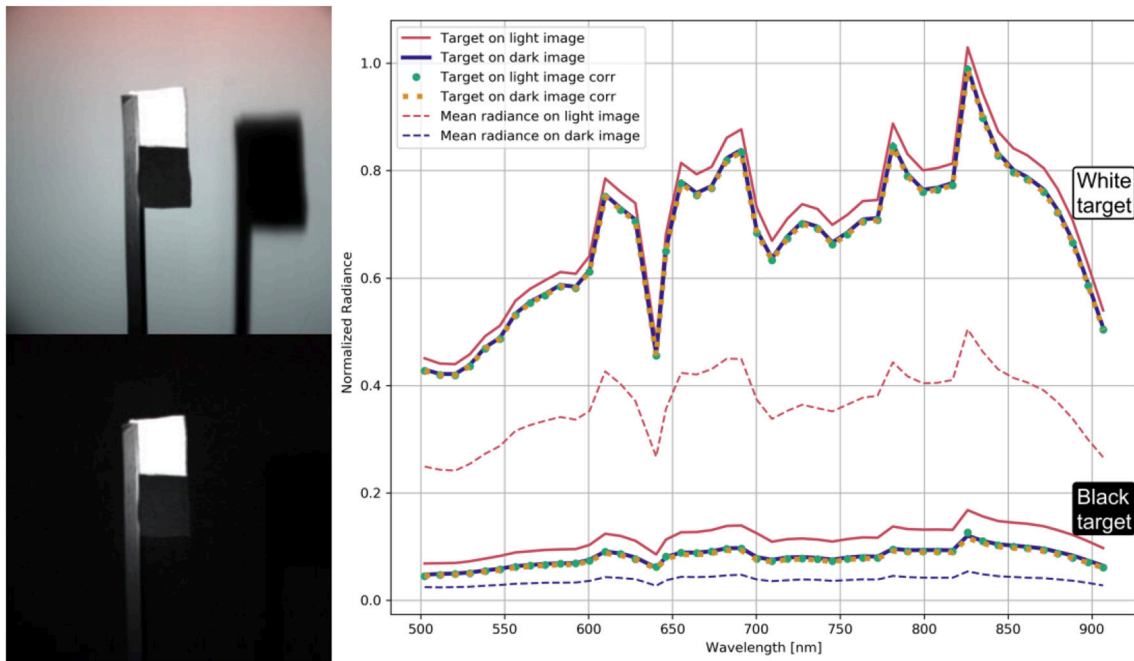


Fig. 10. The images and pseudo radiance spectra acquired in stray light coefficient calibration. The observed radiances of the small targets differ between the light and dark background images due to stray light effects occurring in the optics. After the stray light correction, targets on both images show almost identical radiances.

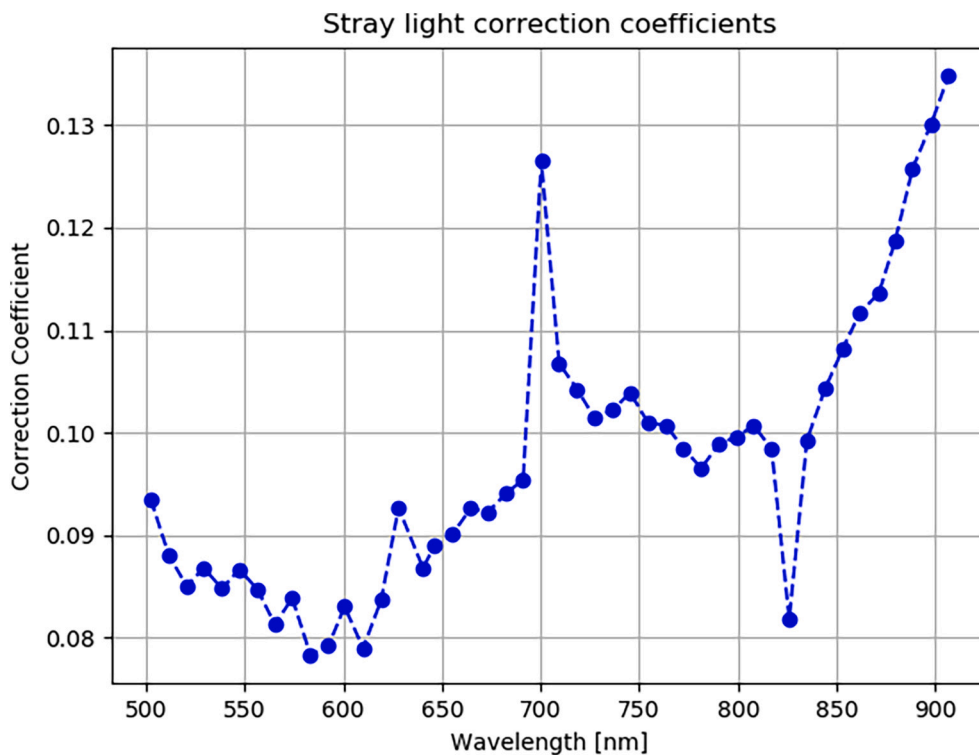


Fig. 11. The stray light coefficient (s_k) for the 46 bands used with the Rikola hyperspectral camera.

more from the reference values.

To quantify the accuracies of the calibration procedures at different heights and spectral range, we computed the NRMSEs for the four reference panels at different flight altitudes intervals with images calibrated without and with atmospheric correction (Table 3). Without atmospheric correction, panels p25 and p50 yielded NRMSEs better than 2.5% for VIS and NIR bands for up to 125 m altitude, and better than 3.7% for altitudes 125–150 m. For the p10, the NRMSEs varied from

2.4%–4.1% in VIS bands and 1.8%–4% in NIR bands for flight heights up to 75 m. However, these values increased to 4%–6.4% in VIS bands and 7.2%–11.8% in NIR bands, for flight altitudes of 75–150 m. For the darkest target (p05), the NRMSEs were 6% for up to 50 m flight altitude and 10.7%–18.5% for NIR bands and 9% for the VIS bands in the 75–150 m altitude interval. After atmospheric correction, the NRMSE of the p05 target improved from 3.5–8.7% to 1.4–2.4%, for VIS bands, and from 2.3–18.5% to 1.5–5%, for NIR bands; the p10 yielded NRMSE of

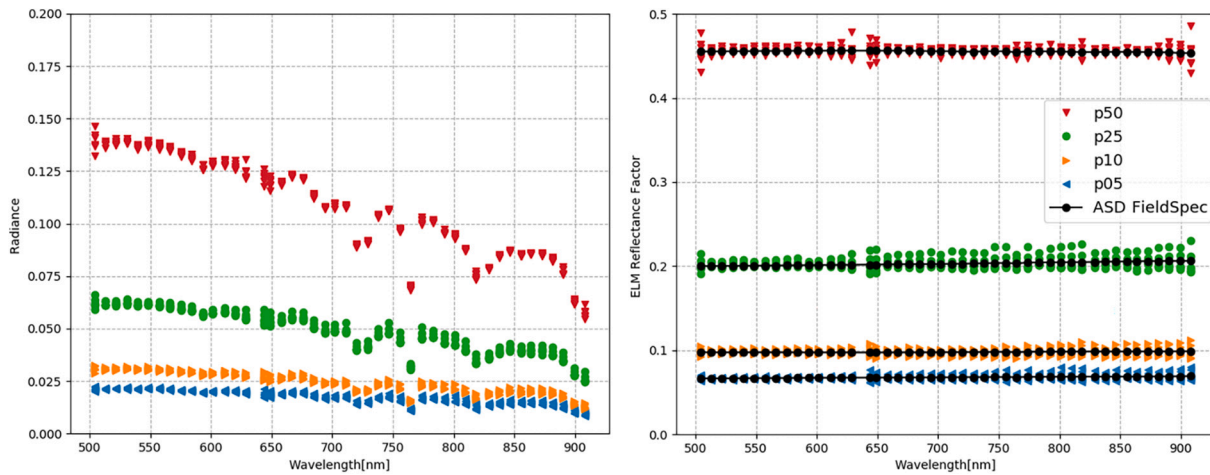


Fig. 12. (Left) Panel radiances picked from six Rikola images during the sunny period of the mapping flight. These images were all good candidates for determining ELM parameters. (Right) Panel reflectance factors calculated using the ELM parameters determined from the p05 and p50 radiances and the ASD FieldSpec in-situ measurements.

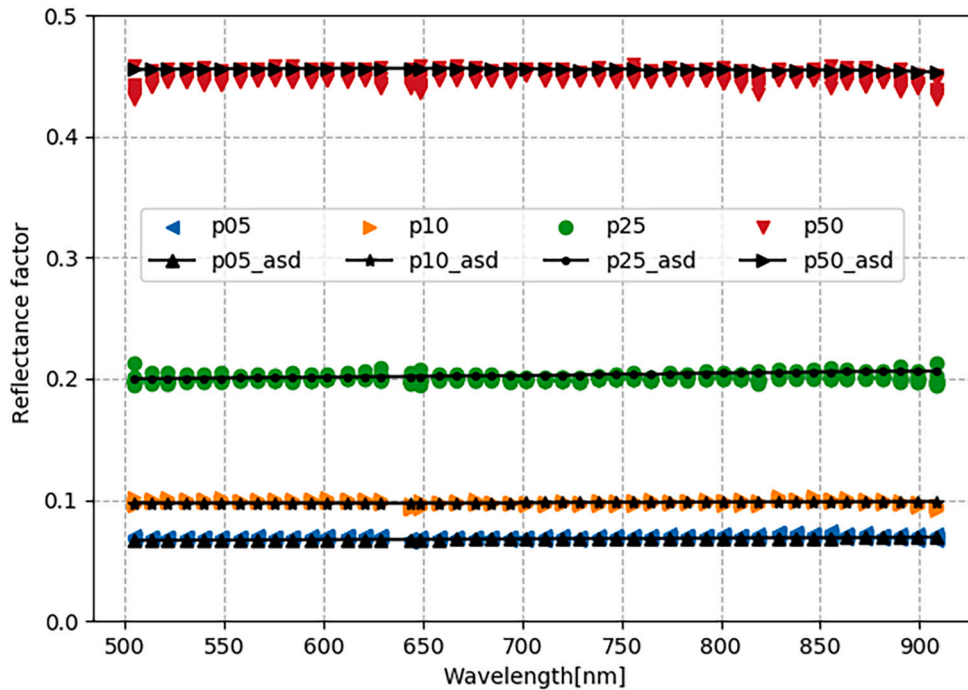


Fig. 13. Reflectance factor spectra of the reference panels as measured on ground using the ASD FieldSpec and as extracted from 9 low-flight-altitude (<30 m) images.

3% for all altitude intervals and spectral ranges. The 50% target had approximately 1% higher NRMSE in the 125–150 m interval than the result without atmospheric correction. Overall, the NRMSEs were at the worst cases 3.1%, 3.7% and 5.3%, respectively, for 75–100 m, 100–125 m, and 125–150 m flight AGL altitudes.

To evaluate the performance of the entire direct reflectance workflow in varying illumination condition, we compared the orthomosaics produced with sunny and cloudy images in 1 m ground sample resolution. We selected a rectangular area of size 50 m by 46 m within the mapping flight area, which included the white and black calibration gravels, agricultural cereal field, and the gravel field with weeds and most of the campaign equipment (Fig. 16). The bottom subplots compare the reflectance factors acquired in sunny and cloudy conditions. The average relative difference for white gravel was +2.8% in VIS and +6.7% in NIR, for black gravel, -5.0% (VIS) and +0.2% (NIR), and

for grain field +0.45% (VIS) and +5.2% (NIR). The largest relative differences of up to 200% appeared in the small areas that were shadowed by tall objects in the sunny data, but to show the more typical smaller errors these get saturated in Fig. 16. The effect of slope can be seen around the ditch that is between the gravel targets and the agricultural field, where the south and north sloping edges of the ditch are showing opposite difference between the sunny and clouded data. Although the vegetated area appears relatively homogenous area in the RGB orthomosaic, it shows large variations in the reflectance factor difference image. This may partly be due to the vegetated area being in the outskirts of the mapping area and the area is not covered well by images from straight above. The shapes of the variations seen in Fig. 16, such as the triangle in the center top and the rectangles in top right corner, follow areas covered by single frames, which suggests that these are orthomosaicking artefacts. Such errors occur due to calibration

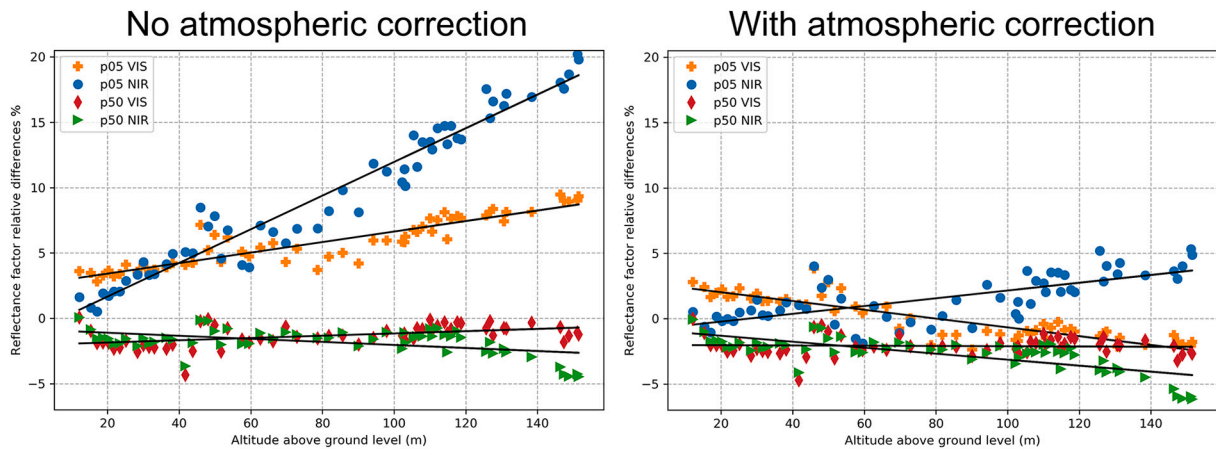


Fig. 14. Effect of altitude on observed reflectance factor without (left) and with (right) atmospheric correction relative to the on-ground spectrometer reference.

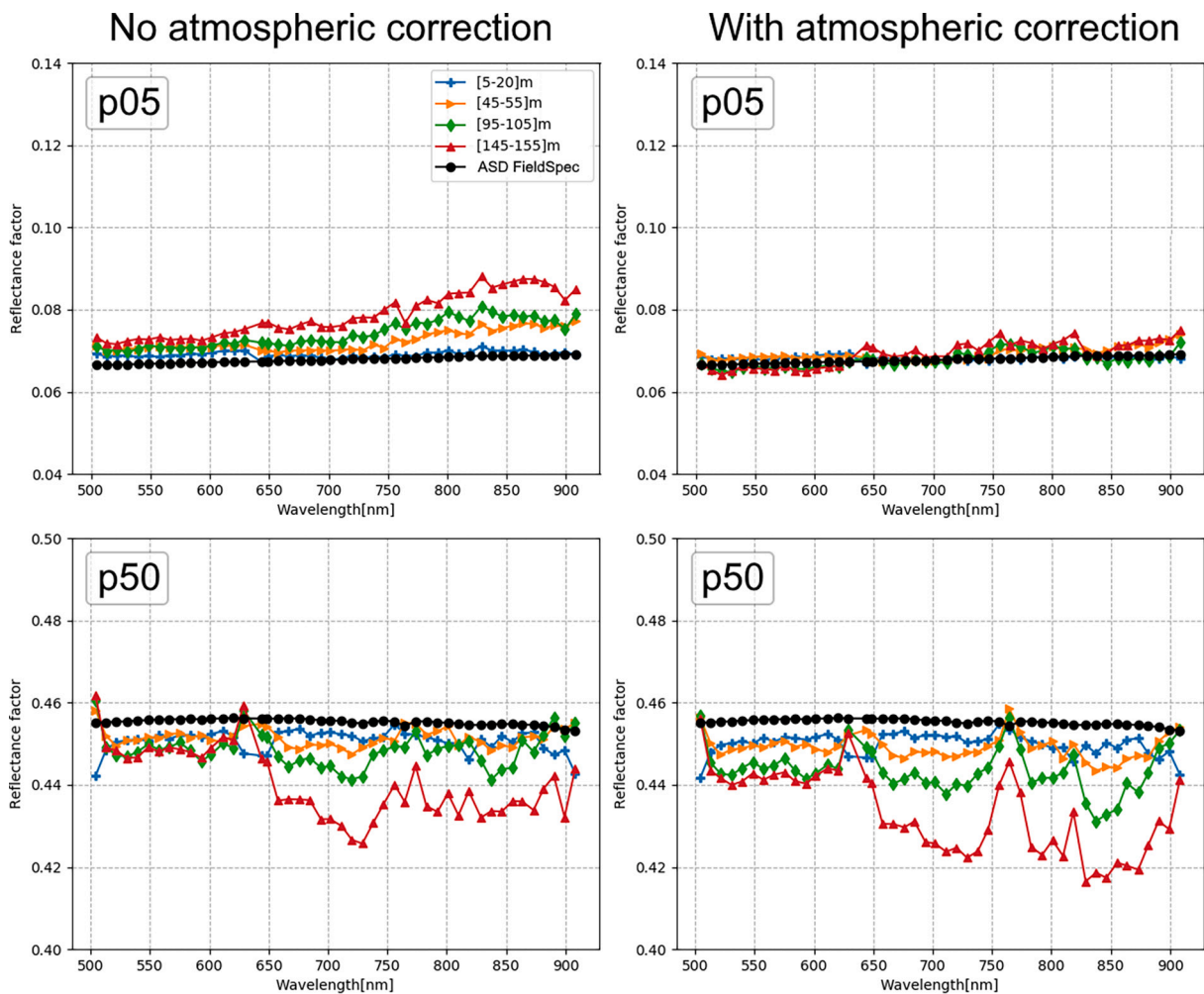


Fig. 15. Reflectance factor spectra of panels p05 (Top) and p50 (Bottom) as measured using the ASD FieldSpec and as extracted from fully sunny elevator flight images at altitude ranges of 5–20 m, 45–55 m, 95–105 m and 145–155 m without (Left) and with (Right) atmospheric correction.

errors in individual frames, but lack of such features in the more central areas of the orthomosaic suggest that these are likely related to strong view angle reflectance anisotropy in vegetation. Similar artefacts are not visible in the gravels, which are located more centrally in the mapping area and that have been specifically selected as the test field calibration targets because they have low reflectance anisotropy effects.

Fig. 17 shows scatter plots of atmospherically corrected reflectance

factors from sunny and cloudy orthomosaics for the area shown in Fig. 15, where each 1-m pixel is one dot. The sunny and cloudy data showed high linear correlation ($R^2 > 0.99$) when the darkest pixels (reflectance < 0.05) were excluded. The darkest pixels were located mostly in the shadowed areas in the sunny data and thus were excluded from the regression statistics as outliers. The pixels in the cloudy images showed systematically approximately 4.3% lower reflectance factors in

Table 3

Error in reflectance factors (NRMSE) acquired in sunny conditions with and without atmospheric correction for each target and altitude range. Units are percentages. The errors larger than 2.5% and 5.0% are highlighted in yellow and red, respectively.

	Altitude interval	VIS					NIR				
		p05	p10	p25	p50	All	p05	p10	p25	p50	All
No atmospheric correction	< 25 m	3.46	2.38	1.20	1.91	2.38	2.30	1.79	1.95	1.66	1.94
	25 m - 50 m	4.72	2.95	1.30	2.30	3.08	6.02	2.57	1.99	2.01	3.57
	50 m - 75 m	5.25	3.60	0.83	1.74	3.33	6.52	3.97	1.45	1.72	3.98
	75 m - 100 m	5.10	4.06	0.99	1.68	3.40	10.69	7.22	1.73	1.92	6.58
	100 m - 125 m	7.13	5.64	1.69	1.40	4.68	13.92	9.70	2.46	2.01	8.63
	125 m - 150 m	8.70	6.38	2.01	1.50	5.54	18.54	11.79	3.15	3.71	11.25
With atmospheric correction	< 25 m	2.26	1.73	1.36	2.06	1.88	1.53	2.20	2.42	1.83	2.03
	25 m - 50 m	2.14	1.50	1.72	2.58	2.03	2.81	2.18	2.81	2.37	2.56
	50 m - 75 m	1.39	0.98	1.42	2.27	1.58	2.40	2.36	2.88	2.40	2.52
	75 m - 100 m	1.93	1.10	2.03	2.45	1.94	3.10	2.71	2.77	2.78	2.85
	100 m - 125 m	1.81	1.32	1.84	2.21	1.82	3.71	2.89	2.32	3.11	3.05
	125 m - 150 m	2.38	1.47	2.12	2.58	2.18	4.93	3.02	2.55	5.28	4.12

VIS and 8.1% lower values in NIR than the corresponding pixels in the sunny images. The atmospheric correction did not have impact in this evaluation.

4. Discussion

Traceable, real-time, and accurate spectral imaging using drones is one of the key future remote sensing technologies. In this research, we developed a calibrated and traceable direct reflectance drone-based hyperspectral imaging system and direct reflectance workflow for photogrammetric and remote sensing applications. Currently, ELM is the most used method for reflectance factor transformation of drone data. However, ELM’s performance is suitable in limited use cases, where there are available appropriate open areas to place the panels, the illumination does not vary too quickly, and the mapped area is small enough (Aasen et al., 2018). In cases where ELM is not suitable, the direct reflectance transformation by means of an on-board irradiance sensor is a truly cost efficient method for quantitative remote sensing.

In our mapping flight test, we showed that the FGI AIRS was able to measure the irradiance on board the drone with the NRMSE of 1.26% in sunny conditions and 1.89% in fully cloudy conditions relative to the ASD FieldSpec irradiance probe on ground. In our previous study, the preliminary assessment in a similar experiment with the old cosine collector optics showed ±2.5% NRMSE error between the AIRS and ASD FieldSpec irradiances (Suomalainen et al., 2018). The improvement in accuracy can be explained by the improved cosine collector optics and calibration, as well as by potentially more stable illumination conditions during the experiment. The AIRS was upgraded with improved cosine collector optics allowing it to measure irradiances onboard drones with absolute accuracy better than ±1.9% at solar zenith angles up to 70°. This can be considered a decent accuracy for an on-board instrument as, e.g., the ASD FieldSpec irradiance probe, in its original form, was found to have up to ±12.5% errors. The AIRS result is slightly worse than the modified ASD FieldSpec probe with ±1.7% errors (our measurement) or the Kipp & Zonen SP Lite2-pyranometer with approximately ±1.5% errors (Kipp and Zonen, 2020) in the same zenith angle range.

Our cosine response measurement on the ASD FieldSpec RCR

irradiance probe raised serious concerns regarding the usability of this device with its original optics, as an accurate irradiance reference system. Our results suggest that users who wish to use their ASD FieldSpec for high accuracy irradiance reference measurements, should check the cosine response of the optics and possibly modify their probe or apply a systematic correction based on the solar zenith angle. As a positive note, with the simple 3D-printed modification ring, we were able to improve the accuracy of our probe to a very acceptable level.

Several remote sensing cameras, such as Headwall cameras, Parrot Sequoia, Micasense cameras, Senop Rikola HSI, MAIA, and Tetracam Mini-MCA, are already equipped with incident light sensors. However, to have any chance for an accurate absolute irradiance measurement on board a drone, a simple irradiance sensor, such as from those cameras, needs to be installed on a stabilized gimbal (Aasen et al., 2018), which in practice are rarely if ever used, or the readings need to be tilt corrected mathematically. For example, Hunt and Stern (2019) used a Tetracam Mini-MCA with its Incident Light Sensor (ILS) onboard a fixed-wing drone for mapping of agricultural fields and reported differences of 27–57% in reflectance factors between flight lines due to tilt of the ILS. Similarly, Hakala et al. (2018) used an unstabilized onboard irradiance sensor on board a multirotor drone and it showed approximately ±8% errors in irradiance readings between opposite flight directions. Bendig et al. (2020), estimated that their onboard irradiance measurement had 1.9% tilt errors in an experiment, where an upward looking irradiance probe was flown on very stable conditions with only 2° tilts. On commercially available solutions, the MicaSense DLS (“Downwelling Light Sensor”) and DLS2 are irradiance sensors that utilize mathematical tilt corrections. The DLS uses a simple correction based on the diffuse/direct irradiance ratio and sun-sensor angle, while the DLS2 employs multiple tilted irradiance sensors in similar fashion as the AIRS does. Mamaghani and Salvaggio (2019b) measured and showed the cosine response of the DLS. Although, they did not draw the conclusion, from their figure it is possible to estimate that the DLS underestimated the irradiance by 4–14% at 40° solar zenith angle and by 30–40% at 70°, indicating that cosine response of the optics has not been properly optimized in the DLS design. Although such large cosine errors make the DLS practically unsuitable for direct reflectance workflow, it can still be

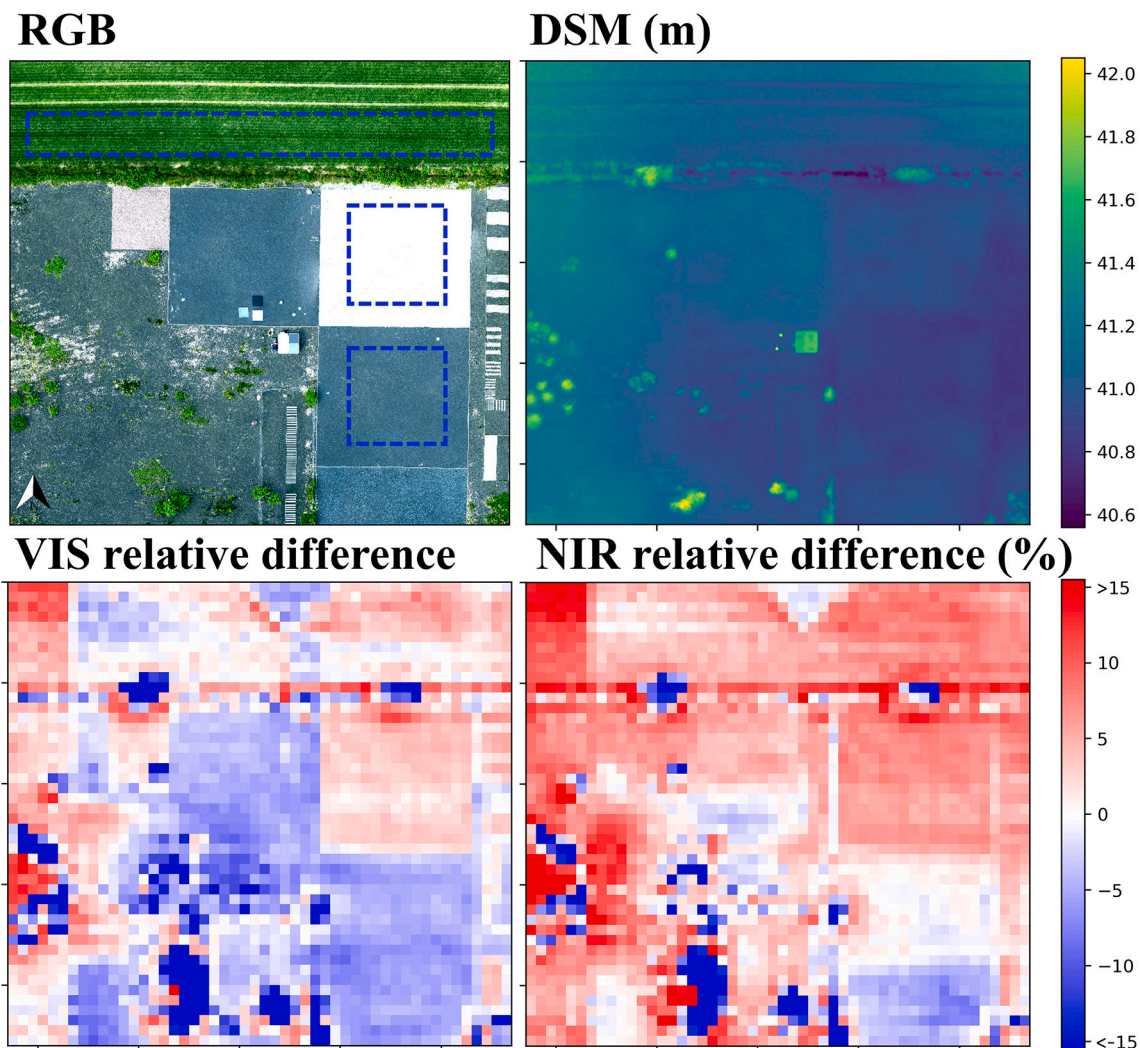


Fig. 16. Comparison between sunny and cloudy atmospherically corrected reflectance factors. Top left: RGB orthomosaic; the white and black gravel and vegetation targets are outlined with dashed line. Top right: Digital Surface Model; Bottom: Relative difference in reflectance factors (sunny minus cloudy) in VIS and NIR bands scaled between -15 to 15% (relative differences were up to 200% in shadows).

a useful tool, if combined with the ELM, for correction of relative changes in illumination during the mapping flight. Such a method has been demonstrated in e.g. [Barker et al. \(2019\)](#), where they observed that for their DLS the largest adjustments would be for the blue and NIR bands. To our knowledge, such cosine response data on the newer DLS2 has not been published, but the official instruction from MicaSense still states that: “In addition to the DLS or sunshine sensor, we strongly recommend that you continue to use a calibrated reflectance panel every time you collect data” ([MicaSense, 2020b](#)). Thus, the MicaSense DLSs, even with their tilt correction, and most of the other incident light sensors sold with other remote sensing cameras, do not seem to be devices designed for absolute irradiance measurements. Thus, they are not suitable for stand-alone direct reflectance processing and not directly comparable to the AIRS as they always require at least single-panel ELM to be used. We hope that, in upcoming years, the remote sensing camera manufacturers would introduce and demonstrate use of true direct reflectance capable irradiance sensors.

In this paper, we also presented the procedure for absolute calibration of the hyperspectral camera, which included corrections for the dark signal, exposure time, stray light, and flat field effects. The Rikola hyperspectral camera was found to have -0.20 ms offset between the nominal and effective exposure time. Although the technical reason why such an offset exists remains unknown to us, by applying the correction,

we were able to remove the effect of camera exposure time in produced radiances. The camera was also found to suffer from stray light, which was equivalent to $8\text{--}13\%$ of the average image intensity. The stray light calibration and correction are not commonly done for drone remote sensing cameras as for most users, the two-point ELM would automatically remove such stray light effects, but the correction is required with direct reflectance processing where absolute radiances are required. If the stray light effects are significant, such calibration would also be necessary in single-panel ELM workflows. Finally, with the high-quality flat field and absolute calibrations, the camera was enabled to produce accurate, absolute, and traceable at-sensor radiances.

To act as reference to the direct reflectance transformation method, we tested the accuracy of the traditional 2-point ELM on the sunny period of the mapping flight dataset. The sunny period had very stable illumination with variation of only $\pm 0.8\%$ providing near ideal conditions for ELM. In the analysis we separated the errors in determining the ELM parameters from the errors in target observation. Firstly, the panels p50 and p05 were used to determine the ELM parameters. In the 6 images observing the panels almost straight down, the p50 and p05 panel radiances on images had standard deviations between 0.5% and 5.2% , with larger errors occurring especially on the darker panel and in NIR bands. These standard deviations represent error in a normal ELM use case where only a single image is used for determining the ELM

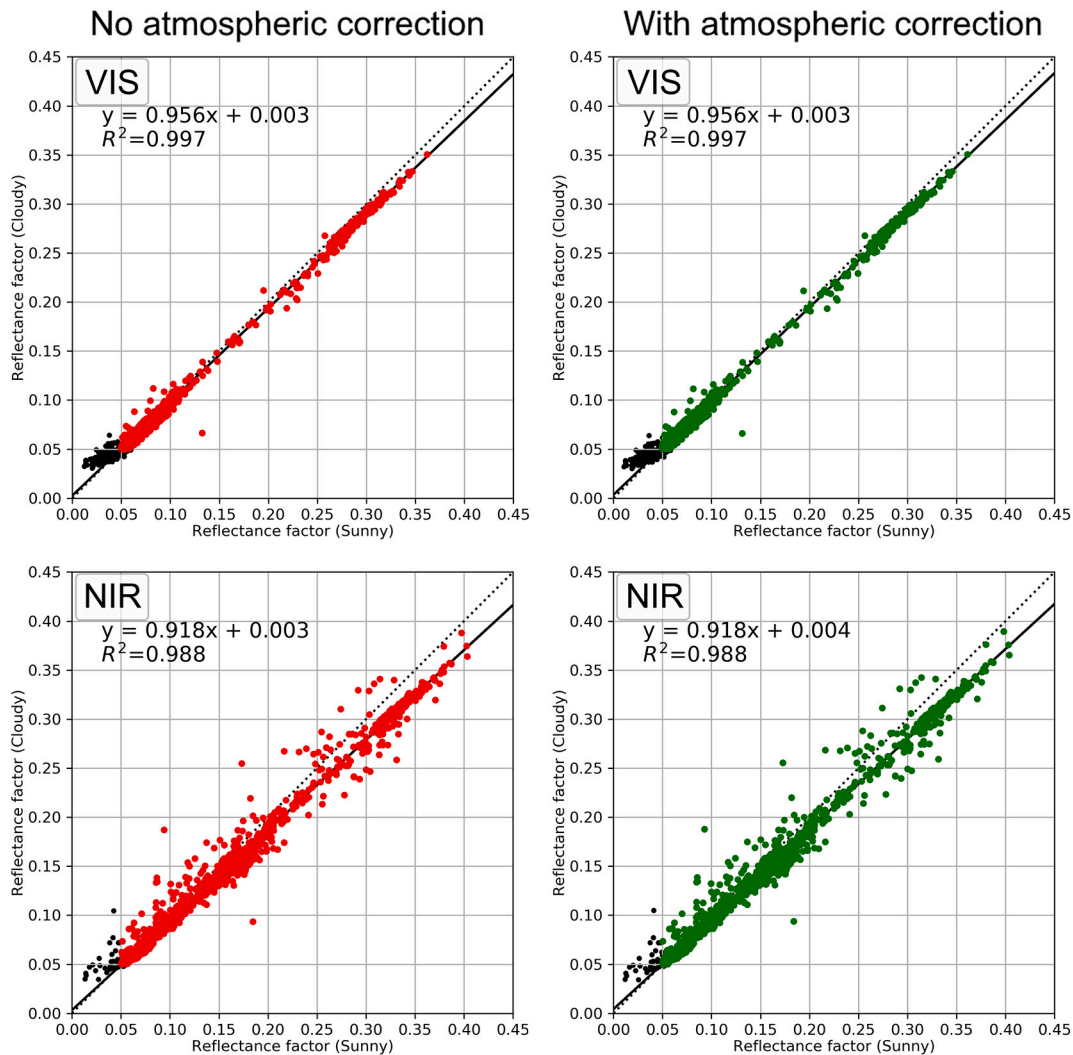


Fig. 17. Pixel-by-pixel comparison of the reflectance factors in the sunny and cloudy orthomosaics in VIS and NIR bands. With darkest pixels excluded (Refl <0.05), the both sunny and cloudy reflectance factor show high linear correlation ($r > 0.99$). The cloudy pixels show systematically approximately 4.3% lower reflectance factors in VIS and 8.1% lower values in NIR than the corresponding sunny pixels.

parameters. These observed variations may be partially due to noise and instability in the camera, but also the small deviations from the nadir view angle geometry can cause such significant errors. Secondly, in the assessment of the ELM reflectance factors, the panels p25 and p10 showed NRMSE errors between $\pm 2.0\%$ and $\pm 4.8\%$, again with larger errors occurring especially on the darker panel and in NIR bands. By combining uncertainties in determining the ELM parameters and in target observation using propagation of error, the total ELM errors in our experiment fall between $\pm 2.1\%$ and $\pm 7.1\%$, depending on the wavelength and the brightness of the target. These results are applicable only in the stable sunny conditions during the experiment and don't take in to account errors e.g. in applicability of the calibration panel reflectances. In a typical ELM use case, the reflectance factors of the calibration panels are not measured in-situ, but an earlier reflectance measurement is used. This introduces additional errors to the ELM reflectances, as the reflectances of all panels vary significantly with the solar zenith angle, the cleanness of the panels may be different from the reflectance measurement, and the panels may not be installed perfectly horizontal. Taking these additional errors and the very stable illumination condition during the experiment into account, especially the error of $\pm 2.0\%$ can be considered to be the best case scenario for ELM and in typical operational usage the error is bound to be much higher.

The accuracies of the direct reflectance factors acquired at very low

altitudes were assessed using the proposed calibration procedure and the four reference panels. Considering all panels imaged at altitudes below 25 m, the NRMSE was less than 2.5%. Jakob et al. (2017) presented an ELM workflow for a similar Rikola HSI camera using manufacturer's radiometric calibration and evaluated its usability in drone-based mineral mapping applications. Their results showed with many samples over 50% deviations between airborne and field reflectance values, indicating some issues in the image calibration or the ELM reflectance conversion process. However, the spectral shapes produced using their method were reasonably good (R^2 : 0.85–0.99) and in the related article (Booyesen et al., 2020) they showed that the method is good enough for mapping of rare earth elements. Minařík et al. (2019) carried out radiometric calibration method based on a laboratory radiometric properties and vicarious correction using an empirical line for a Tetracam μ MCA multispectral camera. The NRMSEs after processing all corrections ranged from 0.24 to 2.10% for images acquired at 15 m altitude. Burkart et al. (2014) pointed out a high correlation ($r^2 > 0.99$) in reflectance between UAV point spectrometers measurements at 10 m altitude and the reference from ASD. Their ASD data varied with an average standard deviation of 4.1% while the UAV data presented average standard deviation of 0.59% of the UAV, which they stated to be due to the much larger footprint of the UAV spectrometer. Gautam et al. (2020) flew a point spectrometer system at 10 m altitude and obtained

relative surface reflectance factors with errors of 5%–7% in the green region, 4%–6% in the red region, 2%–7% around the red edge, and 3%–6% in the NIR.

In our tests at higher imaging altitudes, the atmospheric effects became significant and varied with the altitude and the wavelength. Without atmospheric correction, the bright panels p25 and p50 presented in average 2.5% NRMSEs for altitudes up to 125 m, and increased to 3.7% for altitudes 125–150 m. However, for the dark panels the errors increased significantly when increasing the altitude. Also, the effect was considerably higher for NIR bands than in VIS. For instance, p05 had at the 150 m altitude NRMSE of 18.6% in NIR bands, while VIS presented NRMSE of 8.7%. Guo et al. (2019) also observed similar atmospheric effects with respect to altitude and wavelengths for a multispectral camera MCA 6. A possible reason for the differences between VIS and NIR in our results can be the diffuse light coming from the surrounding vegetation, in the test site, which reflects highly in the NIR, and low in the VIS. Considering flight altitudes of 50–100 m, which are commonly used in agricultural applications, such atmospheric effects could influence the uncertainties of vegetation indices used for crop analyses. Based on our results, the atmosphere starts to significantly affect the signal especially on dark targets already at 50 m flight altitude. The ELM with two or more reflectance reference panels can correct for these effects, but the single-panel ELM, suggested by many drone camera manufacturers, will experience similar errors as seen in our experiment, if no additional atmospheric correction is applied. Our proposed atmospheric correction method can also be used for correction of single-panel ELM data.

By applying the proposed atmospheric correction, our relative accuracies of p05 at altitude range 125–150 m improved from 3.5–8.7% to 1.4–2.4% for VIS bands, and from 2.3–18.6% to 1.5–5.0% for NIR bands. Overall, considering all panels and altitudes up to 150 m, NRMSE was 1.0–2.6% for VIS bands and 1.5–5.3% for NIR bands. Previous research has investigated the use of irradiance spectrometers onboard drones in order to transform the camera radiance to reflectance. (Mamaghani and Salvaggio, 2019b) compared the reflectance transformation using ELM and an irradiance sensor for MicaSense RedEdge-3 for different altitudes (46 m, 69 m, 91 m, 114 m). Their results showed that ELM produced better estimates than their direct reflectance method. For the altitude of 45 m, their average signed reflectance error using the DLS sensor was approximately -0.021 (std ± 0.04), while at the highest altitude (114 m) the average reflectance error was about -0.039 (std ± 0.072). Yang et al. (2017) obtained 5% error in the radiometric calibration of a snapshot hyperspectral camera using ELM for reflectance transformation. In Hunt and Stern (2019) the direct reflectance factors acquired using a TetraCam Mini-MCA and its ILS differed from Landsat 8 OLI reflectances by more than 20%. Edwards et al. (2019) reported reflectance factor accuracy of 6–12%, for Parrot Sequoia, when comparing the standard manufacturer's process, which uses a "sunshine sensor" and a reference panel measurement before and after the flight, to the airborne ELM. Similarly, Cao et al. (2019) tested accuracies of standard MicaSense RedEdge and Airinov MultiSpec 4C workflows against in-situ reflectances and found out that "the accuracy of the raw reflectance values may be low." Compared to these other reported accuracies, the accuracy of the proposed direct reflectance method outperforms most standard camera manufacturer's processes and is aligned in accuracy with the conventional two-panel ELM approach.

We also tested the performance of the proposed direct reflectance workflow in varying cloud conditions. When comparing the sunny and cloudy orthomosaics pixel-by-pixel, the non-shadowed pixels (refl > 0.05) showed high linear correlation ($R^2 > 0.988$). The pixels that showed lower than 0.05 reflectance factor were mostly pixels shadowed by 3D objects in the field in sunny data, and can be considered as outliers in the analysis. The pixels on the cloudy orthomosaic showed systematically lower reflectance factors (-4.3% in VIS and -8.1% in NIR) than their sunny counterparts. The possible measurement error explanations for this disparity could be inaccurate atmospheric correction and

nonlinearities in the radiance/irradiance measurements. However, these are not likely explanations. Firstly, the atmospheric correction had virtually no effect on the disparity. Secondly, our thorough calibrations rule out any camera radiance nonlinearity effects. With the irradiance measurement, the imperfect cosine response of optics would cause such nonlinearity errors when illumination geometry switches between directional (sunny) and isotropic (cloudy). Our cosine calibration results (Table 2) showed that with the original ASD RCR optics such a change from 49° solar zenith angle directional to isotropic geometry, would cause -5% signed error in irradiance measurement. However, with the improved ASD optics this error should be only -1.3% and with AIRS optics only -0.7% . Additionally, our irradiance data shows that the irradiances of ASD and AIRS agree with better than 2% accuracy both in sunny and clouded illuminations. With technical reason ruled out, the observed difference is most likely caused by the natural reflectance anisotropy effects that occur in the targets. The reflectance anisotropies (or Bidirectional Reflectance Distribution Function, BRDF) of the Sjököulla black and white reflectance-target gravels have earlier been measured with the FIGIFIGO instrument (Suomalainen et al., 2009) and have been published by Peltoniemi et al. (2009) as "Black_Gravel" and "White_Gravel2". Unfortunately, the measurements were taken only on one solar zenith angle and they do not allow accurate estimation of isotropic reflectance factors, but the data shows that the gravels in general are darkest when observed from nadir and get brighter at sloped view angles especially in backscattering direction. In the published data, we can see that with the white gravel the directional effects are larger than 15% and with black gravel over 100% relative to the nadir view. Kimes et al. (1987) studied errors on determining the albedo of the targets using the directional reflectance observations. Albedo is closely related to the hemispherical-directional reflectance factor that is observed in the cloudy images, and in their results of vegetated targets at 50° solar zenith angle the directional (sunny) reflectance factor differs from the albedo between -20% and $+50\%$ depending on the vegetation density and leaf angle. Relative to the variations shown in the FIGIFIGO measurements and Kimes et al. albedo results, it seems plausible that the 4.3% and 8.1% discrepancies in sunny and cloudy reflectance factors can be explained by illumination geometry effects.

5. Conclusions

In this study, we demonstrated all steps necessary to develop a rigorous direct method for reflectance transformation, which is one of the greatest bottlenecks in multi- and hyperspectral drone remote sensing. To allow direct reflectance processing, we carried out thorough laboratory calibrations for the irradiance sensor (AIRS) and the hyperspectral frame camera. Absolute irradiance accuracy of the FGI AIRS was enhanced by redesigning and optimizing the cosine responses of the incident light optics. The images of Rikola hyperspectral camera were calibrated with corrections for the dark signal, exposure time, stray light, and flat field effects, and field experiments were used to verify the accuracy of calibration. The experiments suggest that, in the direct reflectance workflow, even a visibly clear atmosphere significantly affects drone image data, and the effects can be seen especially with low-reflectance targets already at 50-m flight altitude. The proposed atmospheric correction method was found to be practical in field use and provided accurate reflectance factors throughout different altitudes and wavelengths. The method requires the use of two reflectance reference panels placed at the take-off or mapping area, but, unlike in ELM, the correction is not affected by the illumination changes e.g. due to clouds. Although not tested yet in this study, following the theory the panels can also be placed more freely than in the ELM, e.g. in a narrow forest opening or even in a shadowed area, with only requirement being that both panels are illuminated similarly. Our results showed that the proposed direct reflectance workflow can provide reflectance factors with accuracy similar to the multi-panel ELM, while being suitable also for long-range BVLOS flights extending far from the calibration panels. The

drone direct reflectance methodology was found to be efficient and being advantageous especially in cases where ELM is not practical, such as in forest monitoring or in large-scale autonomous mapping tasks.

The onboard irradiances were found to have better than 2% accuracy both in sunny and cloudy conditions. The evaluation datasets were selected so that both the images and the irradiance sensor of the drone were both either in direct sunlight or cloud shadow. The method would not be able to do a good correction e.g. in cases where terrain is partially shadowed by clouds or where the clouds cast shadows differently on the irradiance sensor than on the scene down below. Calibrating images acquired in such conditions would be more complex and require introduction of cloud shadow detection algorithms and more indirect estimation of pixelwise irradiances. If such methods are not available in the processing chain, the authors can only suggest discarding of the partially illuminated images from analysis. Furthermore, our results confirmed that the object reflectance anisotropy behaved differently under different conditions, which should be accounted for in further developments.

However, even with the partially illuminated images removed, combining the well-calibrated sunny and clouded reflectance factor images may introduce unwanted variations. Our study showed that, the target reflectance factors acquired in fully sunny and cloudy conditions had up to 8% systematic differences. This disparity was likely to be due to different response of the object reflectance on different illumination conditions, i.e. the object reflectance anisotropy. The reflectance anisotropy effects where view direction and solar zenith angle affect the reflectance factor of targets are already well acknowledged by the satellite and airborne remote sensing communities, but direct reflectance capable drone systems introduce a practical question on comparability of sunny and cloudy reflectance factors. Naturally the areas affected by shadows cast by e.g. trees and other tall objects give completely different reflectance factor in sunny and clouded condition, but also more subtle BRDF effects can change the observed reflectance factors on significant magnitude, as our results showed. If the direct reflectance drone systems are used in varying illumination conditions, the reflectance anisotropy characteristics of the objects, instead accuracy of measurement technique, may be the limiting factor for best possible accuracy of quantitative remote sensing. Improving the accuracy beyond this would require introduction of BRDF corrections that handle also illumination geometry changes to the drone workflow.

Author contribution

J.S. and R.O. were the main authors of the paper, and are responsible for the analysis and results. All authors participated in development of the workflow, discussing the studies, and commenting on the manuscript. J.S. T.H. R.O. N.K. L.M. and R.N. performed the calibrations and acquired the experimental data. E.H. conceptualized and supervised the research, contributed to writing of the manuscript, and arranged funding for the research.

Declaration of Competing Interest

The authors declare that they have no competing financial interests or personal relationships that could have appeared to influence the work reported in this paper.

Acknowledgments

The research leading to these results was funded through the Metrology for Earth Observation and Climate project (MetEOC-3), grant number 16ENV03 within the European Metrology Programme for Innovation and Research (EMPIR) and through the Academy of Finland project "Autonomous tree health analyzer based on imaging UAV spectrometry (Aspect)" (Decision number 327861). The EMPIR is jointly funded by the European Union and the participating countries. Authors

thank A. Kokka, T. Pulli, P. Kärhä and E. Ikonen of Metrology Research Institute (Aalto University, Finland) and MIKES Metrology (VTT Technical Research Centre of Finland) for providing flat field calibration for the hyperspectral camera.

References

- Aasen, H., Honkavaara, E., Lucieer, A., Zarco-Tejada, P., Aasen, H., Honkavaara, E., Lucieer, A., Zarco-Tejada, P.J., 2018. Quantitative remote sensing at ultra-high resolution with UAV spectroscopy: a review of sensor technology, measurement procedures, and data correction workflows. *Remote Sens.* 10, 1091. <https://doi.org/10.3390/rs10071091>.
- Barker, J.B., Woldt, W.E., Wardlow, B.D., Neale, C.M.U., Maguire, M.S., Leavitt, B.C., Heeren, D.M., 2019. Calibration of a common shortwave multispectral camera system for quantitative agricultural applications. *Precis. Agric.* <https://doi.org/10.1007/s11119-019-09701-6>.
- Barreto, M.A.P., Johansen, K., Angel, Y., McCabe, M.F., 2019. Radiometric assessment of a UAV-based push-broom Hyperspectral camera. *Sensors* 19, 4699. <https://doi.org/10.3390/s19214699>.
- Bendig, J., Gautam, D., Malenovsky, Z., Lucieer, A., 2018. Influence of cosine corrector and uas platform dynamics on airborne spectral irradiance measurements. In: *IGARSS 2018–2018 IEEE International Geoscience and Remote Sensing Symposium*. Presented at the *IGARSS 2018–2018 IEEE International Geoscience and Remote Sensing Symposium*, pp. 8822–8825. <https://doi.org/10.1109/IGARSS.2018.8518864>.
- Bendig, J., Malenovsky, Z., Gautam, D., Lucieer, A., 2020. Solar-induced chlorophyll fluorescence measured from an unmanned aircraft system: sensor Etaloning and platform motion correction. *IEEE Trans. Geosci. Remote Sens.* 58, 3437–3444. <https://doi.org/10.1109/TGRS.2019.2956194>.
- Booyens, R., Jackisch, R., Lorenz, S., Zimmermann, R., Kirsch, M., Nex, P.A.M., Gloaguen, R., 2020. Detection of REEs with lightweight UAV-based hyperspectral imaging. *Sci. Rep.* 10, 17450. <https://doi.org/10.1038/s41598-020-74422-0>.
- Burkart, A., Cogliati, S., Schickling, A., Rascher, U., 2014. A novel UAV-based ultra-light weight spectrometer for field spectroscopy. *IEEE Sensors J.* 14, 62–67. <https://doi.org/10.1109/JSEN.2013.2279720>.
- Burkart, A., Aasen, H., Alonso, L., Menz, G., Bareth, G., Rascher, U., 2015. Angular dependency of Hyperspectral measurements over wheat characterized by a novel UAV based goniometer. *Remote Sens.* 7, 725–746. <https://doi.org/10.3390/rs70100725>.
- Cao, S., Danielson, B., Clare, S., Koenig, S., Campos-Vargas, C., Sanchez-Azofeifa, A., 2019. Radiometric calibration assessments for UAS-borne multispectral cameras: laboratory and field protocols. *ISPRS J. Photogramm. Remote Sens.* 149, 132–145. <https://doi.org/10.1016/j.isprsjprs.2019.01.016>.
- Clark, B., Suomalainen, J., Pellikka, P., 2010. A comparison of methods for the retrieval of surface reflectance factor from multitemporal SPOT HRV, HRVIR, and HRG multispectral satellite imagery. *Can. J. Remote. Sens.* 36, 397–411. <https://doi.org/10.5589/m10-071>.
- Cubert, 2020. *Hyperspectral Cameras*. WWW Document. CubertGmbH. URL <https://cubert-gmbh.com/cubert-spectral-cameras/> (accessed 6.2.20).
- Dash, J.P., Watt, M.S., Pearce, G.D., Heaphy, M., Dungey, H.S., 2017. Assessing very high resolution UAV imagery for monitoring forest health during a simulated disease outbreak. *ISPRS J. Photogramm. Remote Sens.* 131, 1–14. <https://doi.org/10.1016/j.isprsjprs.2017.07.007>.
- de Oliveira, R.A., Tommaselli, A.M.G., Honkavaara, E., 2016. Geometric calibration of a Hyperspectral frame camera. *Photogramm. Rec.* 31, 325–347. <https://doi.org/10.1111/phor.12153>.
- Del Pozo, S., Rodríguez-González, P., Hernández-López, D., Felipe-García, B., 2014. Vicarious radiometric calibration of a multispectral camera on board an unmanned aerial system. *Remote Sens.* 6, 1918–1937. <https://doi.org/10.3390/rs6031918>.
- Edwards, J., Anderson, J., Stuart, W., Woolard, J., 2019. An evaluation of reflectance calibration methods for UAV spectral imagery. *Photogramm. Eng. Remote. Sens.* 85, 221–230. <https://doi.org/10.14358/PERS.85.3.221>.
- Gautam, D., Lucieer, A., Bendig, J., Malenovsky, Z., 2020. Footprint determination of a Spectroradiometer mounted on an unmanned aircraft system. *IEEE Trans. Geosci. Remote Sens.* 58, 3085–3096. <https://doi.org/10.1109/TGRS.2019.2947703>.
- Guo, Y., Senthilnath, J., Wu, W., Zhang, X., Zeng, Z., Huang, H., 2019. Radiometric calibration for multispectral camera of different imaging conditions mounted on a UAV platform. *Sustainability* 11, 978. <https://doi.org/10.3390/su11040978>.
- Hakala, T., Markelin, L., Honkavaara, E., Scott, B., Theocharous, T., Nevalainen, O., Näsi, R., Suomalainen, J., Viljanen, N., Greenwell, C., Fox, N., Hakala, T., Markelin, L., Honkavaara, E., Scott, B., Theocharous, T., Nevalainen, O., Näsi, R., Suomalainen, J., Viljanen, N., Greenwell, C., Fox, N., 2018. Direct reflectance measurements from drones: sensor absolute radiometric calibration and system tests for Forest reflectance characterization. *Sensors* 18, 1417. <https://doi.org/10.3390/s18051417>.
- Headwall Photonics, 2020. *Hyperspectral Sensors* [WWW Document]. URL <https://www.headwallphotonics.com/hyperspectral-sensors> (accessed 6.2.20).
- Heinemann, S., Siegmann, B., Thonfeld, F., Muro, J., Jedmowski, C., Kemna, A., Kraska, T., Müller, O., Schultz, J., Udelhoven, T., Wilke, N., Rascher, U., 2020. Land surface temperature retrieval for agricultural areas using a novel UAV platform equipped with a thermal infrared and multispectral sensor. *Remote Sens.* 12, 1075. <https://doi.org/10.3390/rs12071075>.
- Hernández-López, D., Felipe-García, B., Sánchez, N., González-Aguilera, D., Gomez-Lahoz, J., 2012. Testing the Radiometric Performance of Digital Photogrammetric

- Images: Vicarious vs. Laboratory Calibration on the Leica ADS40, a Study in Spain. *Photogramm. Fernerkund. Geoinformation* 557–571. <https://doi.org/10.1127/1432-8364/2012/0139>.
- Honkavaara, E., Peltoniemi, J., Ahokas, E., Kuittinen, R., Hyyppä, J., Jaakkola, J., Kaartinen, H., Markelin, L., Nurminen, K., Suomalainen, J., 2008. A permanent test field for digital photogrammetric systems. *Photogramm. Eng. Remote. Sens.* 1, 95–106. <https://doi.org/10.14358/PERS.74.1.95>.
- Honkavaara, E., Saari, H., Kaivosoja, J., Pölonen, I., Hakala, T., Litkey, P., Mäkinen, J., Pesonen, L., 2013. Processing and assessment of spectrometric, stereoscopic imagery collected using a lightweight uav spectral camera for precision agriculture. *Remote Sens.* 5, 5006–5039. <https://doi.org/10.3390/rs5105006>.
- Honkavaara, E., Rosnell, T., Oliveira, R., Tommaselli, A., 2017. Band registration of tuneable frame format hyperspectral UAV imagers in complex scenes. *ISPRS J. Photogramm. Remote Sens.* 134, 96–109. <https://doi.org/10.1016/j.isprsjprs.2017.10.014>.
- Hunt, E.R., Stern, A.J., 2019. Evaluation of incident light sensors on unmanned Aircraft for Calculation of spectral reflectance. *Remote Sens.* 11, 2622. <https://doi.org/10.3390/rs11222622>.
- Iqbal, F., Lucieer, A., Barry, K., 2018. Simplified radiometric calibration for UAS-mounted multispectral sensor. *Eur. J. Remote Sens.* 51, 301–313. <https://doi.org/10.1080/22797254.2018.1432293>.
- Jakob, S., Zimmermann, R., Gloaguen, R., 2017. The need for accurate geometric and radiometric corrections of drone-borne Hyperspectral data for mineral exploration: MEPHySto—A toolbox for pre-processing drone-borne Hyperspectral data. *Remote Sens.* 9, 88. <https://doi.org/10.3390/rs9010088>.
- Jay, S., Baret, F., Dutartre, D., Malatesta, G., Héno, S., Comar, A., Weiss, M., Maupas, F., 2019. Exploiting the centimeter resolution of UAV multispectral imagery to improve remote-sensing estimates of canopy structure and biochemistry in sugar beet crops. *Remote Sens. Environ.* 231, 110898. <https://doi.org/10.1016/j.rse.2018.09.011>.
- Jiang, J., Zheng, H., Ji, X., Cheng, T., Tian, Y., Zhu, Y., Cao, W., Ehsani, R., Yao, X., 2019. Analysis and evaluation of the image preprocessing process of a six-band multispectral camera mounted on an unmanned aerial vehicle for winter wheat monitoring. *Sensors* 19, 747. <https://doi.org/10.3390/s19030747>.
- Kimes, D.S., Sellers, P.J., Diner, D.J., 1987. Extraction of spectral hemispherical reflectance (albedo) of surfaces from nadir and directional reflectance data. *Int. J. Remote Sens.* 8, 1727–1746. <https://doi.org/10.1080/01431168708954813>.
- Kipp, Zonen, 2020. SP Lite2 pyranometer - Kipp & Zonen [WWW Document]. URL: <https://www.kippzonen.com/Product/9/SP-Lite2-Pyranometer#.XtYUHzozaUk> (accessed 6.2.20).
- Kokka, A., Pulli, T., Honkavaara, E., Markelin, L., Kärhä, P., Ikonen, E., 2019. Flat-field calibration method for hyperspectral frame cameras. *Metrologia* 56, 055001. <https://doi.org/10.1088/1681-7575/ab3261>.
- Mäkinen, J., Holmlund, C., Saari, H., Ojala, K., Antila, T., 2011. Unmanned aerial vehicle (UAV) operated megapixel spectral camera. In: *Electro-optical Remote Sensing, Photonic Technologies, and Applications V*. Presented at the Electro-optical Remote Sensing, Photonic Technologies, and Applications V. International Society for Optics and Photonics, p. 81860Y. <https://doi.org/10.1117/12.897712>.
- Mamaghani, B., Salvaggio, C., 2019a. Multispectral sensor calibration and characterization for sUAS remote sensing. *Sensors* 19, 4453. <https://doi.org/10.3390/s19204453>.
- Mamaghani, B., Salvaggio, C., 2019b. Comparative study of panel and panelless-based reflectance conversion techniques for agricultural remote sensing. [arXiv:1910.03734 \[eess.IV\]](https://arxiv.org/abs/1910.03734).
- MicaSense, 2020a. Sensor Comparison. WWW Document. MicaSense, URL: <https://micasense.com/compare-sensors/> (accessed 6.2.20).
- MicaSense, 2020b. Light Sensors: The Basics (DLS and Sunshine Sensor). WWW Document. MicaSense Knowl. Base. URL: <https://support.micasense.com/hc/en-us/articles/115002782008> (accessed 6.2.20).
- Minařík, R., Langhammer, J., Hanuš, J., 2019. Radiometric and atmospheric corrections of multispectral μ MCA camera for UAV spectroscopy. *Remote Sens.* 11, 2428. <https://doi.org/10.3390/rs11202428>.
- Näsi, R., Honkavaara, E., Lyytikäinen-Saarenmaa, P., Blomqvist, M., Litkey, P., Hakala, T., Viljanen, N., Kantola, T., Tanhuanpää, T., Holopainen, M., 2015. Using UAV-based photogrammetry and Hyperspectral imaging for mapping bark beetle damage at tree-level. *Remote Sens.* 7, 15467–15493. <https://doi.org/10.3390/rs71115467>.
- Nevalainen, O., Honkavaara, E., Tuominen, S., Viljanen, N., Hakala, T., Yu, X., Hyyppä, J., Saari, H., Pölonen, I., Imai, N., Tommaselli, A., Nevalainen, O., Honkavaara, E., Tuominen, S., Viljanen, N., Hakala, T., Yu, X., Hyyppä, J., Saari, H., Pölonen, I., Imai, N.N., Tommaselli, A.M.G., 2017. Individual tree detection and classification with UAV-based photogrammetric point clouds and Hyperspectral imaging. *Remote Sens.* 9, 185. <https://doi.org/10.3390/rs9030185>.
- Oliveira, R.A., Khoramshahi, E., Suomalainen, J., Hakala, T., Viljanen, N., Honkavaara, E., 2018. Real-time and post-processed georeferencing for hyperspectral drone remote sensing. In: *ISPRS - International Archives of the Photogrammetry, Remote Sensing and Spatial Information Sciences*. Presented at the ISPRS TC II Mid-term Symposium <q>Towards Photogrammetry 2020</q> (Volume XLII-2) - 4–7 June 2018, Riva del Garda, Italy, Copernicus GmbH, pp. 789–795. <https://doi.org/10.5194/isprs-archives-XLII-2-789-2018>.
- Oliveira, R.A., Näsi, R., Niemeläinen, O., Nyholm, L., Alhonoja, K., Kaivosoja, J., Jauhainen, L., Viljanen, N., Nezami, S., Markelin, L., Hakala, T., Honkavaara, E., 2020. Machine learning estimators for the quantity and quality of grass swards used for silage production using drone-based imaging spectrometry and photogrammetry. *Remote Sens. Environ.* 246, 111830. <https://doi.org/10.1016/j.rse.2020.111830>.
- Ortiz, J.D., Avouris, D., Schiller, S., Luvall, J.C., Lekki, J.D., Tokars, R.P., Anderson, R.C., Shuchman, R., Sayers, M., Becker, R., 2017. Intercomparison of approaches to the empirical line method for vicarious Hyperspectral reflectance calibration. *Front. Mar. Sci.* 4 <https://doi.org/10.3389/fmars.2017.00296>.
- Pekkala, O., Pulli, T., Kokka, A., Ikonen, E., 2019. Setup for characterising the spectral responsivity of Fabry-Pérot-interferometer-based hyperspectral cameras. *Metrologia* 56, 065005. <https://doi.org/10.1088/1681-7575/ab3fd1>.
- Peltoniemi, J., Hakala, T., Suomalainen, J., Puttonen, E., 2009. Polarised bidirectional reflectance factor measurements from soil, stones, and snow. *J. Quant. Spectrosc. Radiat. Transf.* 110, 1940–1953. <https://doi.org/10.1016/j.jqsrt.2009.04.008>.
- Ristorio, G., Mazzetto, F., Guglieri, G., Quagliotti, F., 2015. Monitoring performances and cost estimation of multirotor unmanned aerial systems in precision farming, in: 2015 international conference on unmanned aircraft systems (ICUAS). In: Presented at the 2015 International Conference on Unmanned Aircraft Systems (ICUAS), pp. 502–509. <https://doi.org/10.1109/ICUAS.2015.7152329>.
- Rykowski, R.F., Kreysar, D.F., 2005. *Stray light correction method for imaging light and color measurement system*, p. 6975775.
- Senop, 2020. Hyperspectral Cameras [WWW Document]. URL: <https://senop.fi/en/optronics-hyperspectral> (accessed 6.2.20).
- Smith, G.M., Milton, E.J., 1999. The use of the empirical line method to calibrate remotely sensed data to reflectance. *Int. J. Remote Sens.* 20, 2653–2662. <https://doi.org/10.1080/014311699211994>.
- SPECIM, 2020. Airborne Systems. WWW Document. Specim Airborne Syst. URL: <https://www.specim.fi/airborne/> (accessed 6.2.20).
- Suomalainen, J., Hakala, T., Peltoniemi, J., Puttonen, E., 2009. Polarised multiangular reflectance measurements using the Finnish geodetic institute field Goniospectrometer. *Sensors* 9, 3891–3907. <https://doi.org/10.3390/s90503891>.
- Suomalainen, J., Anders, N., Iqbal, S., Roerink, G., Franke, J., Wenting, P., Hünninger, D., Bartholomeus, H., Becker, R., Kooistra, L., 2014. A lightweight Hyperspectral mapping system and photogrammetric processing chain for unmanned aerial vehicles. *Remote Sens.* 6, 11013–11030. <https://doi.org/10.3390/rs6111013>.
- Suomalainen, J., Hakala, T., Alves de Oliveira, R., Markelin, L., Viljanen, N., Näsi, R., Honkavaara, E., 2018. A novel tilt correction technique for irradiance sensors and spectrometers on-board unmanned aerial vehicles. *Remote Sens.* 10, 2068. <https://doi.org/10.3390/rs10122068>.
- Tetracam, 2020. Multispectral Imaging Systems [WWW Document]. URL: <http://www.tetracam.com/ImagingSystems.htm> (accessed 6.2.20).
- Topcon, 2016. HiPer HR. WWW Document. Topcon Position. Syst. Inc. URL: <https://www.topconpositioning.com/gnss-and-network-solutions/integrated-gnss-recorders/hiper-hr> (accessed 6.8.20).
- Vermote, E.F., Tanre, D., Deuze, J.L., Herman, M., Morcette, J.-J., 1997. Second simulation of the satellite signal in the solar Spectrum, 6S: an overview. *IEEE Trans. Geosci. Remote Sens.* 35, 675–686. <https://doi.org/10.1109/36.581987>.
- Wallace, L., Lucieer, A., Watson, C., Turner, D., 2012. Development of a UAV-LIDAR system with application to Forest inventory. *Remote Sens.* 4, 1519–1543. <https://doi.org/10.3390/rs4061519>.
- Wang, C., Myint, S.W., 2015. A simplified empirical line method of radiometric calibration for small unmanned aircraft systems-based remote sensing. *IEEE J. Sel. Top. Appl. Earth Obs. Remote Sens.* 8, 1876–1885. <https://doi.org/10.1109/JSTARS.2015.2422716>.
- Wilson, R.T., 2013. Py6S: a Python interface to the 6S radiative transfer model. *Comput. Geosci.* 51, 166–171. <https://doi.org/10.1016/j.cageo.2012.08.002>.
- Ximea, 2020. Hyperspectral Cameras [WWW Document]. URL: <https://www.ximea.com/en/usb3-vision-camera/hyperspectral-usb3-cameras-mini>.
- Yang, G., Li, C., Wang, Y., Yuan, H., Feng, H., Xu, B., Yang, X., Yang, G., Li, C., Wang, Y., Yuan, H., Feng, H., Xu, B., Yang, X., 2017. The DOM generation and precise radiometric calibration of a UAV-mounted miniature snapshot Hyperspectral imager. *Remote Sens.* 9, 642. <https://doi.org/10.3390/rs9070642>.
- Zarco-Tejada, P.J., González-Dugo, V., Berni, J.A.J., 2012. Fluorescence, temperature and narrow-band indices acquired from a UAV platform for water stress detection using a micro-hyperspectral imager and a thermal camera. *Remote Sens. Environ.* 117, 322–337. <https://doi.org/10.1016/j.rse.2011.10.007>.